Economic Geology, v. 112, pp. 1483–1507

Hydrothermal Rare Earth Element (Xenotime) Mineralization at Maw Zone, Athabasca Basin, Canada, and Its Relationship to Unconformity-Related Uranium Deposits

Morteza Rabiei,[1] Guoxiang Chi,[1,†] Charles Normand,[2] William J. Davis,[3] Mostafa Fayek,[4] and Nigel J.F. Blamey[5]

[1] *Department of Geology, University of Regina, 3737 Wascana Parkway, Regina, Saskatchewan S4S 0A2, Canada*

[2] *Saskatchewan Geological Survey, Saskatchewan Ministry of Economy, 1000-2103 11th Avenue, Regina, Saskatchewan S4P 3Z8, Canada*

[3] *Geological Survey of Canada, 601 Booth Street, Ottawa, Ontario K1A 0E8, Canada*

[4] *Department of Geological Sciences, University of Manitoba, 240 Wallace Building, 125 Dysart Road, Winnipeg, Manitoba R3T 2N2, Canada*

[5] *Department of Earth Sciences, Brock University, 1812 Sir Isaac Brock Way, St. Catharines, Ontario L2S 3A1, Canada*

Abstract

The Maw zone rare earth element (xenotime) deposit is hosted in brecciated sandstones in the Athabasca Basin and is associated with silicification, hematitization, and tourmalinization (magnesiofoitite). Petrographic studies indicate that xenotime precipitated after significant compaction of the host rocks and was coeval with the main phase of tourmaline and drusy quartz. Sensitive high-resolution ion microprobe U-Pb dating of xenotime yielded a $^{207}Pb/^{206}Pb$ age of 1547 ± 14 Ma. In situ secondary ion mass spectrometry oxygen isotope analysis of coeval tourmaline and quartz gives temperatures from 89° to 385°C (average 185°C) and $\delta^{18}O_{VSMOW\text{-}Fluid}$ values from –6.2 to +10.8‰ (average +1.6‰). The coexistence of different types of fluid inclusions (liquid-dominated biphase, vapor-dominated biphase, vapor only, and halite-bearing triphase) in individual fluid inclusion assemblages in drusy quartz suggests boiling and heterogeneous trapping. Excluding the heterogeneously entrapped fluid inclusions, the liquid-dominated biphase inclusions yielded homogenization temperatures from 63° to 178°C, ice-melting temperatures mainly from –37.4° to –21.8°C, and salinities mainly from 22.0 to 28.3 wt %. Raman spectroscopic and mass spectrometric analyses indicate low nonaqueous volatile concentrations (<1 mole %). In conjunction with regional stratigraphy indicating burial depth less than 2.5 km at the time of mineralization, these data suggest an epithermal mineralization environment. The similarities in wall-rock alteration, paragenesis, mineralization age, oxygen isotopes, and fluid inclusion attributes between the Maw zone rare earth element deposit and unconformity-related uranium deposits in the region invokes a possible genetic link between them. The hydrothermal fluid at Maw zone probably represents one of the fluids that carried reducing agents and caused uraninite precipitation in the unconformity-related uranium deposits.

Introduction

Rare earth element (REE) mineralization occurs in a variety of geologic environments, including carbonatite and alkaline igneous complexes, iron oxide copper-gold (IOCG) deposits, various pegmatites, porphyry molybdenum deposits, uranium-REE skarn deposits, migmatized gneisses, sedimentary phosphorites, uraniferous and auriferous pyritic quartz pebble conglomerates (paleoplacers), placers, and weathering residue of REE-rich precursors (granite-associated laterites and bauxites; Long et al., 2010). Although currently the most important REE producers are those associated with carbonatite and granite-derived laterite, significant REE resources are present in sedimentary basins, mainly in placers, paleoplacers, and phosphorites (Long et al., 2010). In addition to these sedimentary REE deposits, authigenic REE mineralization (mainly consisting of xenotime) has also been reported in many sedimentary basins, e.g., the Proterozoic Birrindudu Basin in Australia (Vallini et al., 2007; Hoatson et al., 2011) and the Athabasca Basin in Canada (Harper, 1987; Quirt et al., 1991; Normand, 2014), but the nature, scope, and economic potential of the authigenic REE mineralization remain to be fully understood.

†Corresponding author: e-mail, Guoxiang.Chi@uregina.ca

It is widely recognized that most REE mineralization is associated with anomalously elevated concentrations of U and Th, to the extent that the radioactivity in REE ore wastes becomes a major environmental problem (Long et al., 2010). The Olympic Dam IOCG deposit, which is rich in REEs, is also known for its enormous uranium resource (Hitzman and Valenta, 2005; Jefferson et al., 2007). Elevated concentrations of REEs are commonly encountered in uranium deposits, such as in the unconformity-related uranium deposits in the Athabasca Basin (Normand, 2014). As sedimentary-hosted uranium deposits are the most important source of uranium (Kyser and Cuney, 2009; Fayek, 2013), it is of both economic and scientific interest to investigate the genetic relationship between REE and U mineralization in sedimentary basins.

The Athabasca Basin in northern Saskatchewan, Canada (Fig. 1), which hosts numerous high-grade, unconformity-related uranium deposits (Jefferson et al., 2007; Kyser and Cuney, 2009; Fayek, 2013), contains a number of occurrences of light and heavy rare earth elements (Normand, 2014). These REE occurrences include local concentrations of detrital monazite and zircon, as well as REE mineralization associated with diagenetic and hydrothermal uranium oxides, aluminum-phosphate-sulfate (APS) minerals, apatite, and xenotime (e.g., Fayek, 1996; Gaboreau et al., 2007; Normand, 2014). Most unconformity-related uranium deposits in the

doi: 10.5382/econgeo.2017.4518
0361-0128/17/1483-25

Submitted: February 5, 2017
Accepted: May 24, 2017

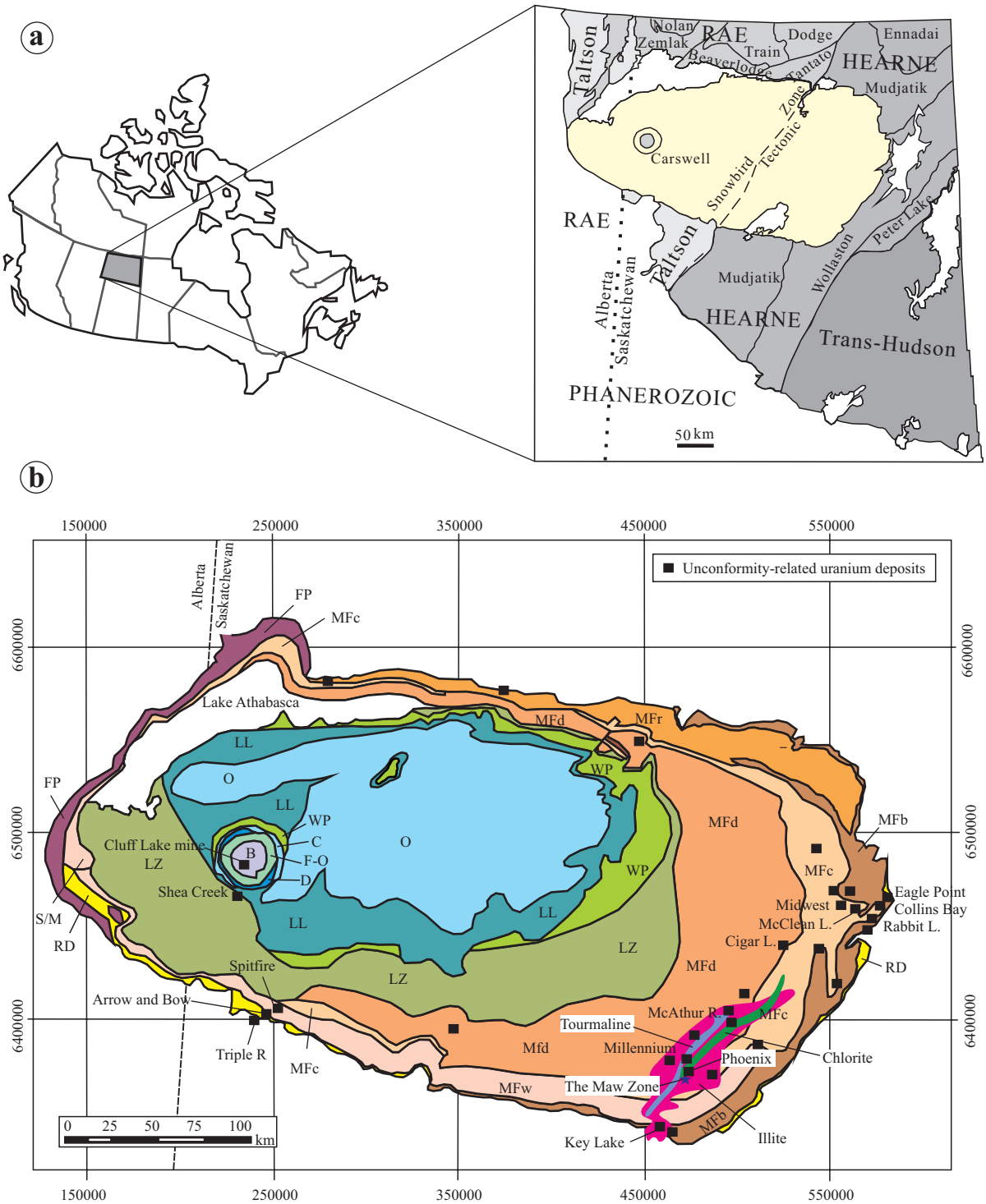

Fig. 1. (a) Location of the Athabasca Basin in the regional tectonic framework of northern Saskatchewan's Precambrian (after Card, 2012). (b) Regional geologic map of the Athabasca Basin showing each formation, major uranium deposits (modified from Jefferson et al., 2007; Ramaekers et al., 2007; Bosman et al., 2012), and the location of regional illite, chlorite, and tourmaline anomalies in the surficial material and outcrops of the Athabasca Group (after Earle and Sopuck, 1989). Abbreviations: B = basement, C = Carswell, D = Douglas, F - O = undivided Fair Point to Otherside formations, FP = Fair Point, LL = Locker Lake, LZ = Lazenby Lake, MF = Manitou Falls (b = Bird, c = Collins, d = Dunlop, r = Raibl, w = Warnes), O = Otherside, RD = Read, S/M = undifferentiated Smart and/or Manitou Falls, W = Wolverine Point. The map grid coordinates are given in the UTM, North American Datum 1983 (NAD83), zone 13N.

Athabasca Basin contain elevated concentrations of REEs. The uraninite in these deposits contains ~0.1 to 2.0 wt % total REEs (ΣREE), of which the majority (88% on average) is composed of heavy REEs (HREEs) and yttrium (Fayek and Kyser, 1997; Jefferson et al., 2007; Mercadier et al., 2011; Normand, 2014). However, it remains unclear whether or not the unconformity-related uranium mineralization and the REE mineralization are genetically related.

The Maw zone REE (xenotime) deposit, located in the southeastern part of the Athabasca Basin and spatially close to several unconformity-related uranium deposits (Fig. 1), provides a good opportunity to examine the genesis of authigenic xenotime mineralization, as well as its relationship with uranium mineralization. A number of studies have been carried out for this deposit, including local geology, petrography, mineralogy, and geochemistry (MacDougall, 1990; Quirt et. al., 1991; Hanly, 2001; Barker, 2007; Pan et al., 2013; Chen et al., 2016). However, key factors related to the formation of the deposit, including the age of mineralization and the temperature, pressure, and composition of the ore-forming fluids, have not been examined, and a potential genetic relationship with unconformity-related uranium mineralization remains controversial (Quirt et al., 1991; Pan et al., 2013). It is known that authigenic xenotime in sedimentary basins can be formed from early diagenesis to late diagenetic or hydrothermal stages (Rasmussen, 1996, 2005; McNaughton et al., 1999; Fletcher et al., 2000; England et al., 2001; Vallini et al., 2002; Kositcin et al., 2003; Lan et al., 2013), and so it is crucial to determine the age of the xenotime in the Maw zone deposit in order to understand its origin. The ore-forming fluids of the unconformity-related uranium deposits in the Athabasca Basin have been well characterized through fluid inclusion and stable isotope studies (e.g., Pagel et al., 1980; Kotzer and Kyser, 1995; Derome et al., 2005; Richard et al., 2016; Wang, 2016), and it is important to carry out similar studies for the Maw zone deposit in order to verify if the ore-forming fluids for the different mineralizing systems are genetically related.

The primary objective of this study is to characterize the mineralizing system of the Maw zone deposit through detailed field, petrographic, geochronological, stable isotope, and fluid inclusion studies, to constrain the nature and conditions of the mineralization. Second, we examine possible genetic relationships between the Maw zone REE deposit and the unconformity-related uranium deposits in the region through comparison in paragenesis, age, and characteristics of the ore-forming fluids. The implications of the results of this study for understanding the mineralization processes of the unconformity-related uranium deposits in the Athabasca Basin are also discussed.

Geologic Setting

Regional geologic background

The Athabasca Basin is a Paleoproterozoic to Mesoproterozoic basin developed on Archean to Paleoproterozoic basement rocks in the western Churchill Province (Hoffman, 1988). The western Churchill Province, flanked by two major orogenic belts, i.e., the ca. 1.9 Ga Taltson magmatic zone to the west and the ca. 1.8 Ga Trans-Hudson Orogen to the east, is composed of the Rae and Hearne provinces, separated by the Snowbird tectonic zone, which lies below the central part of the Athabasca Basin (Hoffman, 1988; Card et al., 2007; Fig. 1a). The basement rocks that form the Rae and Hearne provinces consist of Archean granitoid gneiss and metasedimentary and metavolcanic rocks, and overlying Paleoproterozoic metasedimentary rocks (Card et al., 2007). The Hearne Province in Saskatchewan, which underlies the eastern part of the Athabasca Basin where the study area is located, is subdivided into three domains including the Wollaston, Mudjatik, and Virgin River domains (Card et al., 2007; Fig. 1a).

The Athabasca Basin is composed principally of continental quartzose siliciclastic rocks that have not been subjected to metamorphism and significant deformation (Ramaekers et al., 2007). The basin fill, referred to as the Athabasca Group, is divided into four unconformity-bounded sedimentary sequences, namely sequence 1 to sequence 4 from bottom to top (Ramaekers et al., 2007). Sequence 1 consists of the Fair Point Formation, which is developed in the western part of the basin and composed of conglomeratic and pebbly quartz arenite. Sequence 2 comprises the conglomeratic Read Formation in the east and the sandy Smart Formation in the west, and the overlying Manitou Falls Formation, which is mainly composed of quartz arenite and conglomerate. Sequence 3 consists of the Lazenby Lake Formation, which is composed of sandy, conglomeratic and pebbly siliciclastic rocks and the Wolverine Point Formation dominated by mudstone and siltstone. Sequence 4 comprises the Locker Lake Formation, composed of pebbly and conglomeratic sandstone, the Otherside Formation of conglomerate and sandstone, the Douglas Formation of quartz arenite and carbonaceous mudstone, and the Carswell Formation of stromatolite, oolite, and minor siliciclastic interbeds. The age of the Athabasca Basin is constrained to be younger than ca. 1750 Ma and older than ca. 1267 Ma, the former based on thermogeochronological data of the Trans-Hudson Orogen (Annesley et al., 1997; Orrell et al., 1999; Kyser et al., 2000; Alexandre et al., 2009), and the latter on the age of the Mackenzie diabase dikes that cut through the Athabasca Group (LeCheminant and Heaman, 1989). A U-Pb age of 1644 ± 13 Ma was reported for igneous zircon in tuffaceous units in the Wolverine Point Formation (Rainbird et al., 2007), and an Re-Os isochron age of 1541 ± 13 Ma was obtained for carbonaceous shales in the Douglas Formation (Creaser and Stasiuk, 2007).

A number of uranium deposits are developed near the unconformity between the Athabasca Group and the basement, named unconformity-type, unconformity-related, or unconformity-associated uranium deposits (Hoeve and Sibbald, 1978; Hoeve and Quirt, 1984; Jefferson et al., 2007; Kyser and Cuney, 2009; Fayek, 2013). These deposits are closely associated with reactivated basement faults crosscutting the unconformity and with clay alterations (Hoeve and Sibbald, 1978; Hoeve and Quirt, 1984; Thomas et al., 2000; Jefferson et al., 2007; Li et al., 2015). The unconformity-related uranium deposits are distributed in various parts of the basin, but so far the most important ones are mainly located in the eastern part of the basin, especially along the Wollaston-Mudjatik transition zone (WMTZ) within the basement (Fig. 1). An NE-trending alteration corridor, consisting of chlorite, illite, and tourmaline alterations, has been recognized in the southeastern part of the Athabasca Basin (Earle

aind Sopuck, 1989), which encompasses some of the most important uranium deposits in the region (Key Lake, Phoenix, and McArthur River; Fig. 1b) and coincides with a prominent linear topographic feature on the unconformity surface, interpreted to be related to a reactivated basement structure (Li et al., 2015).

Geology of the Maw zone deposit

The Maw zone REE deposit is located between the McArthur River uranium deposit to the northeast and the Key Lake uranium deposit to the southwest, approximately 6 km to the southwest of the Phoenix uranium deposit (Fig. 1b). Together with these uranium deposits, the Maw zone is situated within the regional NE-trending alteration corridor (Fig. 1b) mentioned above. A pre-NI 43-101-compliant resource estimation in the mid 1980s indicated 462,664 tonnes of ores averaging 0.21% Y_2O_3 for the deposit (Knox, 1986; Normand, 2014).

The deposit is hosted in the Manitou Falls Formation of the Athabasca Group, which is divided into, from bottom to top, the Bird (MFb), Collins (MFc), and Dunlop (MFd) members, and is underlain by the Read Formation above the basement (Kerr, 2010; Fig. 2). The mineralization is hosted by a pipe-like brecciated zone (Fig. 2), and is mainly developed in the Collins and Dunlop members of the Manitou Falls Formation, about 130 m above the basal unconformity (Fig. 2). Regionally, the Collins Member is characterized by quartz arenite with less than 1% clay intraclasts and less than 2% conglomerate beds, and the Dunlop Member is characterized by the presence of quartz arenite with more than 1% clay intraclasts (Ramaekers et al., 2007). Within the breccia zone, the Collins and Dunlop members are characterized by variably brecciated and silicified sandstones (Fig. 3).

The breccias are mostly fragment supported, and the fragments are variably sized and subangular (Fig. 3a-c). The fragments are silicified sandstone with variable degrees of hematitization, and the matrix is made of fine sandstone grains cemented by variable amounts of tourmaline, hematite, and quartz (Fig. 3a-c). Quartz occurs as a silicification product in the fragments and matrix as well as drusy crystals in fractures (Fig. 3d). Tourmaline, which was identified as dravite in the literature (Quirt et al., 1991; Hanly, 2001; Cloutier et al., 2010), has a bluish green color (Fig. 3b, c, d), typically occurs as fracture filling (Fig. 3b) and as a cement and replacement product in the matrix (Fig. 3c) and clasts of breccia (Fig. 3d), and commonly is intergrown with drusy quartz in fractures (Fig. 3d). The intensity of alteration (particularly tourmalinization) is proportional to the intensity of brecciation and fracturing (Barker, 2007). Xenotime is not discernable, in most cases, in hand samples from the outcrops or cores. However, locally xenotime aggregates were found as centimeter-sized, brown patches in silicified sandstones (Fig. 3e, f). These mineralized patches are not conformable with the bedding (Fig. 3e, f).

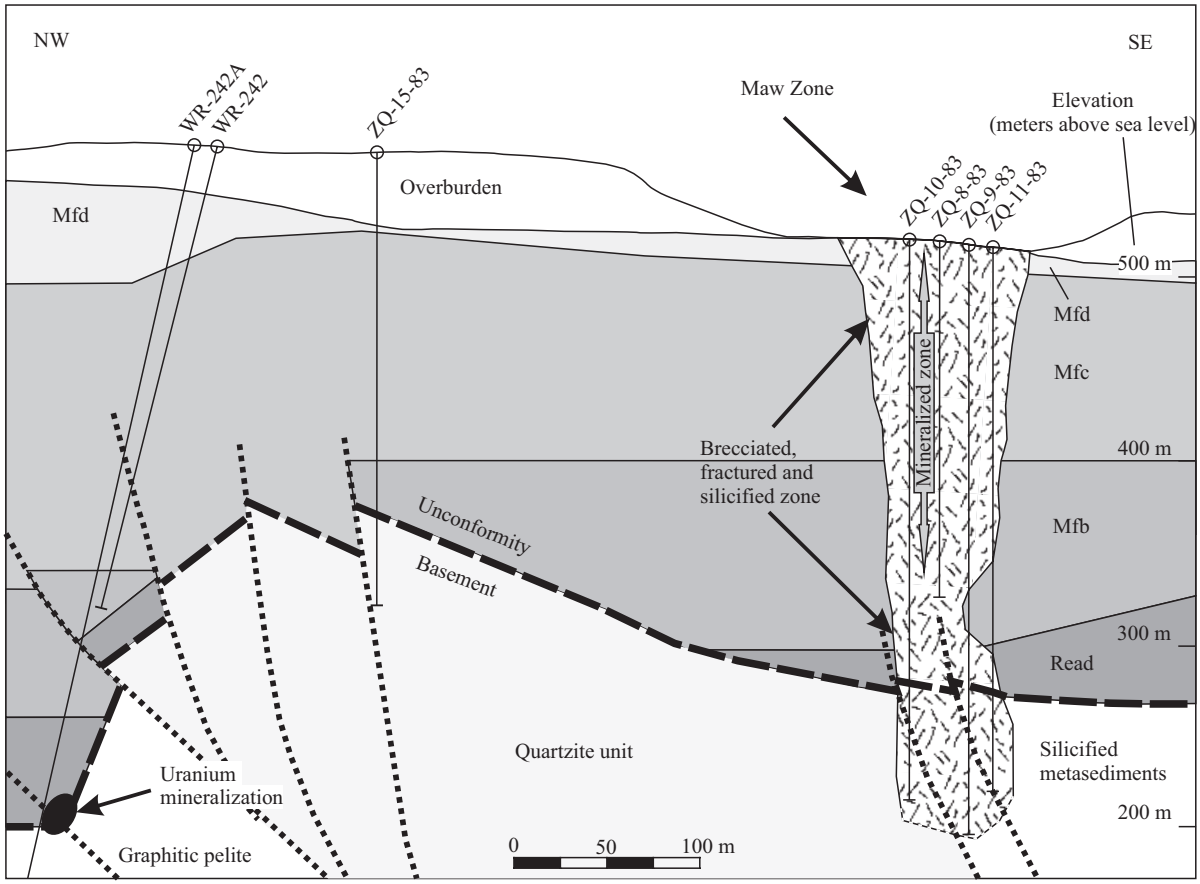

Fig. 2. A schematic cross section of the Maw zone area and its spatial association with the basal unconformity and nearby URU mineralization (modified from Kerr, 2010, and Pan et al., 2013). See Figure 1 caption for abbreviations.

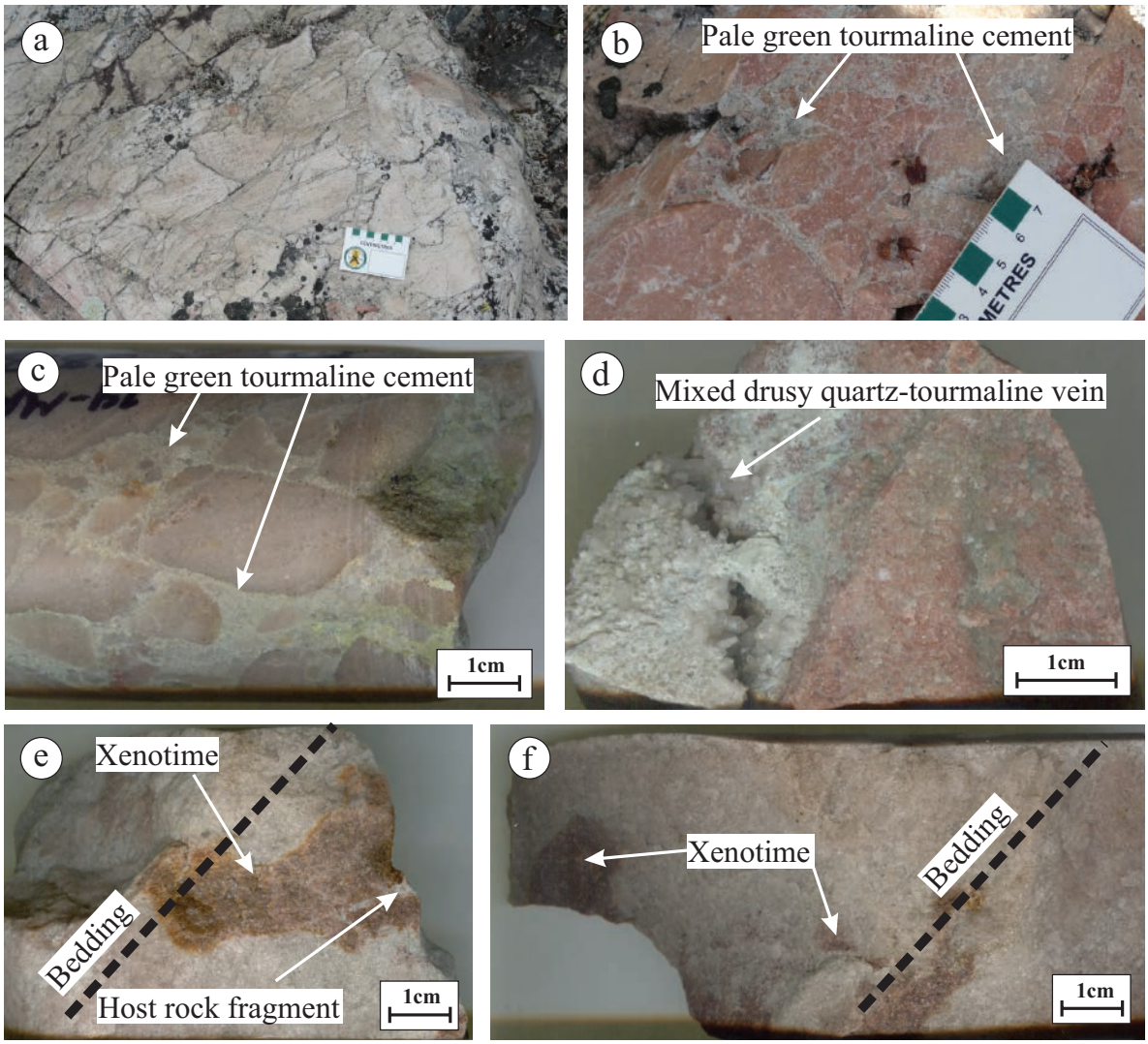

Fig. 3. Photographs showing brecciated sandstones and mineralization in outcrops and core from the Maw zone REE deposit. (a) Fragment-supported and mosaic structures. (b) Brecciated hematitized sandstone with pale green tourmaline cement. (c) Drill core segments composed of sandstone breccia cemented by tourmaline in drill hole 85-01 at depth of 38.8 m. (d) Drill core segment showing the development of tourmaline and drusy quartz in a vein in drill hole ZQ-8-83 at depth of 40.3 m. (e, f) Photographs showing drill core samples that contain massive, brown patches of xenotime from drill hole ZQ-8-83 at depths of 75.0 m (e) and 75.2 m (f).

Analytical Methods

Samples collected from the Maw zone REE deposit were analyzed for petrography, geochronology, stable isotopes, and fluid inclusions. Petrography was conducted on polished thin sections using a conventional petrographic microscope and a scanning electron microscope (SEM). In situ U-Pb isotope dating was done on xenotime using a sensitive high-resolution ion microprobe (SHRIMP). In situ oxygen isotopes were analyzed using a secondary ion mass spectrometer (SIMS) on pairs of quartz and tourmaline showing coprecipitation features, and fluid inclusions in quartz were analyzed by microthermometry, Raman spectroscopy, and mass spectrometry for gases.

Petrography

A detailed petrographic study was conducted on 86 polished thin sections of samples from outcrops and drill cores. Optical examination by transmitted and reflected light was performed using an Olympus BX51 petrographic microscope. A scanning electron microscope equipped for energy-dispersive spectroscopy (EDS) was used as an auxiliary tool to characterize fine-grained minerals. SEM-EDS analysis was carried out at the University of Regina using a JEOL JSM-6360 scanning electron microscope equipped with a Thermo Scientific Noran System 7 energy-dispersive detector.

SHRIMP U-Pb geochronology of xenotime

A polished thin section cut from a xenotime-rich sample was prepared for SHRIMP U-Pb isotope analysis at the Geological Survey of Canada in Ottawa. Areas of interest were cored out of the polished section using a 3-mm-diameter drill core. Individual polished cores were assembled in an epoxy puck (IP771) along with a prepolished plug containing xenotime

standards 6410 and 6413 (Stern and Rayner, 2003). Analyses were conducted using an ^{16}O- primary beam ca. 7 × 9 μm in diameter at 10 kV and ca. 0.7-nA beam current. A common lead correction based on measured count rates of ^{204}Pb utilized the Stacey and Kramers (1975) model lead composition at the measured $^{207}Pb/^{206}Pb$ age. Elemental calibration for $^{206}Pb/^{238}U$ in xenotime analyses by ion probe is subject to significant compositional matrix effects, in particular U and Th + REEs (e.g., Fletcher et al., 2004, 2010). For this reason, a two-stage calibration was employed. The analyses were first calibrated based on correlation of $ln^{206}Pb/^{254}UO$ vs. $ln^{270}UO2/^{254}UO$ and an age of 900 Ma for reference material 6410 using SQUID version 2.2 (Ludwig, 2009). Xenotime 6410 exhibits little compositional variation in uranium and thorium, so potential matrix effects are limited. A calibration error of 1.48% was calculated and applied. A second reference xenotime (6413) with variable U was then utilized to evaluate matrix effects. The strongest effect is due to uranium content. A second correction factor to account for the uranium matrix effect was determined by linear regression of the % deviation from accepted $^{206}Pb/^{238}U$ value against $^{254}UO/^{194}Y_2O$, which is a measure of the uranium content. The correction was then applied to all the $^{206}Pb/^{238}U$ ratios and errors calculated by propagation of the slope and intercept error. The $^{207}Pb/^{235}U$ age was calculated from the corrected $^{206}Pb/^{238}U$ value and the measured $^{207}Pb/^{206}Pb$ value with error propagated.

The analyzed xenotime grains have relatively low uranium and thorium contents, comparable to reference material 6410, and some inaccuracy in the measured $^{206}Pb/^{238}U$ ratios due to other unaccounted-for matrix effects may remain. For this reason, the $^{207}Pb/^{206}Pb$ ages rather than $^{206}Pb/^{238}U$ ages were used for age interpretations. No instrumental mass fractionation correction was applied to the lead isotope data based on measured $^{207}Pb/^{206}Pb$ ages within the error of accepted values for the 6410 (891 ± 12 Ma compared to TIMS value of 900 ± 1.6 Ma) and the 6413 (994 ± 6 Ma compared to 996 ± 0.8 Ma) reference materials.

SIMS oxygen isotope analyses

Oxygen isotope compositions of selected quartz and tourmaline were measured using a CAMECA IMS 7f SIMS housed at the Manitoba Regional Materials and Surface Characterization Facility, University of Manitoba. A ~2-nA primary beam of Cs+ was accelerated at 10 kV and focused to a 10- × 15-μm spot using a 100-μm aperture in the primary column. An offset of 200 volts was used to eliminate molecular ion interferences. Ions were detected with a Balzers SEV 1217 electron multiplier coupled with an ion-counting system using an overall dead time of 52 ns. Two isotopes of oxygen, $^{16}O^-$ and $^{18}O^-$, were detected by switching the magnetic field. Individual analyses comprised 70 cycles and lasted ~10 min. The standard and minerals of interest were analyzed during the same analytical session. The results are reported as $\delta^{18}O_{VSMOW}$ in ‰. Spot-to-spot reproducibility on the quartz and tourmaline standards is better than 0.7‰ and 0.5‰, respectively.

Fluid inclusion analyses

Doubly polished sections about 100 μm in thickness were prepared from representative samples containing drusy quartz crystals. Fluid inclusion petrography was first carried out to assess the types and occurrences of fluid inclusions, with a particular emphasis on the application of the fluid inclusion assemblage (FIA) concept (Goldstein and Reynolds, 1994). Selected fluid inclusions were analyzed using microthermometry and Raman spectroscopy, and bulk fluid inclusions in separate quartz samples were analyzed for gas compositions with mass spectrometry. The technical procedures of each of these methods are described below.

Microthermometric analysis of the fluid inclusions was carried out using a Linkam THMS 600 heating-freezing stage adapted to an Olympus BX 51 microscope. The heating-freezing stage was calibrated using synthetic CO_2-H_2O (CO_2 melting temperature at –56.6°C) and H_2O fluid inclusions (ice melting temperature at 0°C and critical temperature at 374.1°C). The precision was ±0.1°C for measurement of ice or hydrohalite melting temperatures ($T_{m\text{-}ice}$ or $T_{m\text{-}HH}$) if they were the last phase to melt (if ice or hydrohalite was not the last melting phase, their melting temperatures were less precise), and ±1° to 2°C for measurement of total homogenization temperatures. Based on the microthermometric data, the composition of the fluid inclusions was approximated by the H_2O-NaCl-$CaCl_2$ system, and the salinities (NaCl + $CaCl_2$ wt %) and weight fraction of NaCl (i.e., X_{NaCl} = NaCl/(NaCl + $CaCl_2$)) were estimated using the program of Steele-MacInnis et al. (2011).

Raman spectroscopic analysis was conducted using an RM2000 Renishaw laser Raman instrument to evaluate the volatile and solute compositions of individual fluid inclusions. The excitation laser wavelength of the Raman spectroscope was set to 514 nm, the grating used was 1,800 gr/mm, and the objective magnification was ×50. In order to analyze the solute composition, cryogenic Raman analyses were carried out following the procedure described by Chi et al. (2014) and Chu et al. (2016), and the results were compared with published Raman spectra (Baumgartner and Bakker, 2010; Chi et al., 2014, 2017).

Pure drusy quartz crystals were handpicked and cleaned in a potassium hydroxide solution immersed in a Bransonic ultrasonic bath to remove surface contamination. The cleaned quartz crystals were sent for analysis at the New Mexico Institute of Mining and Technology. Two Pfeiffer Prisma quadrupole mass spectrometers operating in the fast-scan and peak-hopping mode were used to analyze the samples, which were crushed incrementally under a vacuum (~10^{-8} Torr) producing six to 10 successive bursts (Norman and Moore, 2003). Capillary tubes filled with commercial Scott Gas gas mixtures of known composition (2% uncertainty) and three in-house fluid inclusion gas standards were used for calibration (Blamey, 2012). The analytical precision was better than 5% for major gas species (CO_2, CH_4, Ar, and N_2) and 10% for minor species (Blamey, 2012).

Petrography and Paragenesis

Petrographic observations of sandstone and breccia samples from Maw zone indicate that the predominant components of these rocks are detrital clasts (mainly quartz with minor muscovite, hematite, and zircon grains), with variable amounts of diagenetic and hydrothermal minerals. The detrital quartz grains are typically rounded and are less than 1 mm in diameter (Figs. 4, 5). Authigenic components occur as cement or

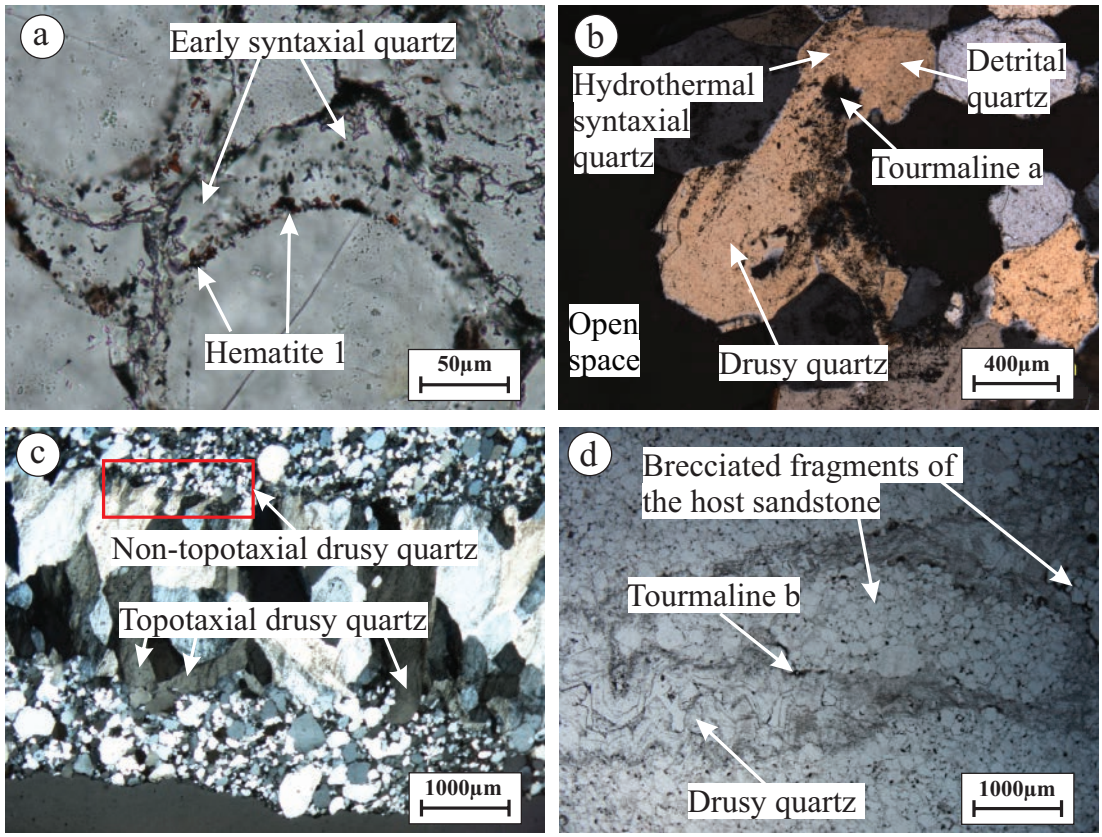

Fig. 4. Photomicrographs showing various features exhibited by different types of quartz. (a) First generation of syntaxial quartz that predates brecciation and encloses flaky hematite (H1) that rims detrital quartz. (b) A photomicrograph (crossed polars) displaying drusy quartz that grew in crystallographic continuity from a second generation of syntaxial quartz (hydrothermal syntaxial quartz). Continuity of growth between hydrothermal syntaxial and drusy quartz is revealed by similar birefringence and extinction. Patches of tourmaline a occur locally at the transition between hydrothermal syntaxial quartz and drusy quartz. (c) A vein consisting of drusy quartz crystals with their long axis perpendicular to the vein wall. (d) Drusy quartz filling open space and cementing brecciated fragments.

replacement in the interstitial space between detrital grains, as replacement overprinting detrital grains, and as open-space filling in fractures and vugs (Figs. 4, 5). The most important authigenic minerals include quartz, tourmaline, hematite, and xenotime. Xenotime is the principal REE-bearing mineral in the Maw zone deposit. The presence of an unidentified HREE- and Y-bearing phase occurring as grains measuring <5 μm in size nucleated on zircon and possible bastnaesite was reported by Chen et al. (2016). Trace amounts of APS minerals have also been reported to occur locally (Chen et al., 2016). The [THREE (Eu to Lu) + Y]/TREE ratios calculated from published bulk geochemical analyses of mineralized rocks from the Maw zone are >0.8 (Normand, 2014), reflecting the predominance of HREE- and Y-rich phases. The main characteristics of the authigenic minerals and their relationships with detrital minerals are described below, followed by a summary of the paragenetic sequence.

Authigenic quartz

Authigenic quartz occurs in two forms: (1) syntaxial quartz (quartz overgrowth) and (2) drusy quartz. Two generations of syntaxial quartz were recognized. The first generation overgrows detrital quartz grains and generally contains iron oxide (Fig. 4a). This phase of syntaxial quartz does not show intergrowth textures with tourmaline and appears to predate tourmalinization. The second generation of syntaxial quartz is much more common than the first and is coeval with the first generation of hydrothermal tourmaline (Fig. 4b); it is hereafter referred to as hydrothermal syntaxial quartz. Two modes of drusy quartz are distinguished: one grew in crystallographic continuity with hydrothermal syntaxial quartz (Fig. 4b) and the other nucleated directly from the walls of fractures without evidence of topotaxy (Fig. 4c). Both types of drusy quartz can form crystals that project into open spaces, develop in veins, and occur as cement in breccia (Fig. 4b-d).

Tourmaline

Tourmalinization is the most prominent type of alteration in the Maw zone deposit (Fig. 3b-d). The tourmaline, which occurs as hair-like, fibrous crystals, was originally identified as dravite, including varieties of chrome dravite (Quirt et al., 1991), alkali-free dravite, and alkali-free chromium dravite (Hanly, 2001). However, recent investigations by O'Connell et al. (2015) and Adlakha and Hattori (2016), for tourmaline from Maw zone as well as the nearby Phoenix and McArthur River uranium deposits, suggest that the alkali-deficient Mg tourmaline should

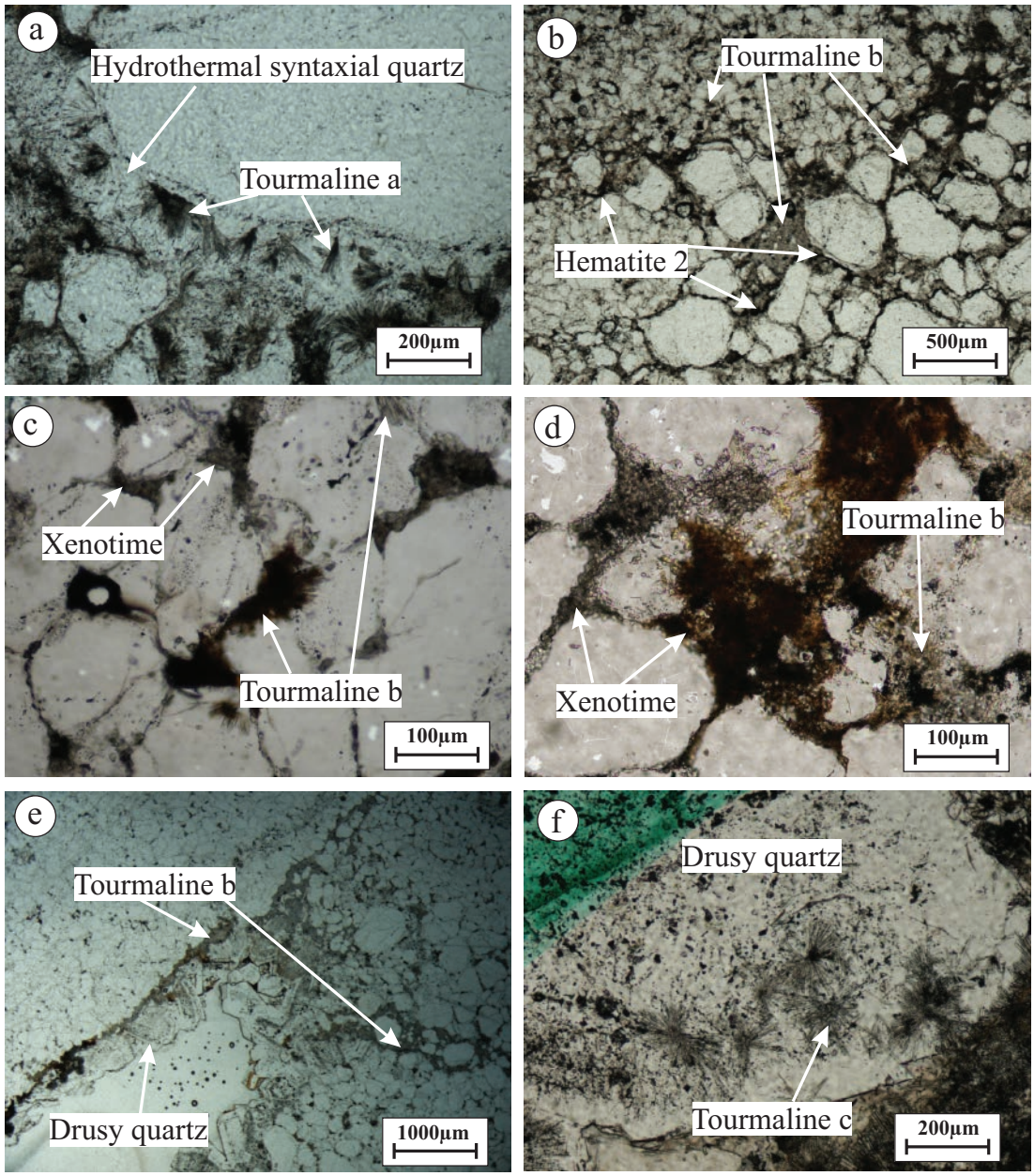

Fig. 5. Photomicrographs showing various modes of occurrence of tourmaline in the Maw zone REE deposit. (a) Photomicrograph showing a second generation of syntaxial quartz (hydrothermal syntaxial quartz) that is accompanied by the formation of early prismatic tourmaline (tourmaline a). (b) Tourmaline b occurring in interstitial space and as cement of breccias. (c, d) Tourmaline and xenotime coexisting between detrital quartz grains. (e) Tourmaline b as a cement of breccias and filling open space. (f) The latest generation of tourmaline (c) occurring within drusy quartz.

be properly classified as magnesiofoitite. In this paper, we use the general term "tourmaline." The tourmaline in the Maw zone can be divided into three phases—a, b, and c—based on their occurrences. The earliest phase (a) occurs locally as needles or rosettes within hydrothermal syntaxial quartz (Fig. 5a). Phase b tourmaline, which is much more abundant than phase a, occurs as aggregates between detrital quartz grains, as a cement in breccia, and filling open spaces (Fig. 5b-e). The latest phase (c), which is of limited distribution, mainly occurs within and intergrown with drusy quartz (Fig. 5f).

Hematite

Several generations of authigenic hematite were identified. The first generation is represented by flakes of hematite (H1) developed on the rims of detrital quartz and enclosed by the early phase of syntaxial quartz (Fig. 5a). The most pervasive phase of hematitization (H2) is coeval with the formation of phase b tourmaline, and occurs between brecciated sandstone fragments and detrital quartz grains (Fig. 5b). The latest generation of hematite (H3) partially fills open space in fractures.

Xenotime

Electron microprobe analyses of xenotime from Maw zone provided by Hanly (2001) indicate that Y^{+3} is the main cation occupying the eightfold coordinated crystallographic sites of the mineral ($X_Y^{VIII} > 0.7$). Xenotime occurs as μm-scale crystals between detrital quartz grains and replaces the latter (Fig. 6a, b), and is coeval with phase b tourmaline (Fig. 6c, d). Where patchy concentrations of xenotime occur in the sandstone, the detrital quartz grains appear to float in a matrix of xenotime (Figs. 6a, 7), which might be taken to suggest that xenotime mineralization precipitated during early diagenesis (before significant compaction). However, careful examination of areas inside and outside of the mineralized patches reveals that the number of detrital grains per view area is similar in both (Fig. 7), indicating that mineralization took place by replacement after compaction.

Paragenetic sequence

A paragenetic sequence, comprising sedimentation, diagenetic, and hydrothermal stages (Fig. 8), was established based on the crosscutting relationships and mineral assemblages described above. Sedimentation of detrital components (quartz, muscovite, zircon, and hematite) was followed, in order, by precipitation of early diagenetic hematite (H1) rimming detrital grains and by the formation of diagenetic quartz overgrowths. During the early stages of hydrothermal activity, a new generation of syntaxial quartz (hydrothermal syntaxial quartz) was developed, which shows a gradual transition to drusy quartz, and minor amounts of tourmaline (phase a) were precipitated. During the main stage of hydrothermal activity, dissolution accompanied by brecciation took place, followed by precipitation of large amounts of drusy quartz, tourmaline (phase b), and hematite (H2), as well as xenotime. Minor amounts of tourmaline (phase c) were precipitated toward the end of the main hydrothermal stage. Hematitization (H3) along fine fractures occurred in the waning stage of hydrothermal activity.

SHRIMP U-Pb Dating of Xenotime

A semimassive patch of xenotime collected from mineralized sandstone in drill hole ZQ-8-83 (at a depth of 75 m) was used to prepare a polished thin section for in situ U-Pb isotope analysis using SHRIMP. The results of 14 analytical spots of xenotime are listed in Table 1. Most of the data plot close to the concordia curve (Fig. 9), but, considering potential matrix effects that may not have been completely accounted for, as explained in the section of study methods, $^{207}Pb/^{206}Pb$ ages rather than $^{206}Pb/^{238}U$ ages are considered more reliable. The $^{207}Pb/^{206}Pb$ ages obtained have a weighted mean of 1547 ± 14 Ma (Fig. 9).

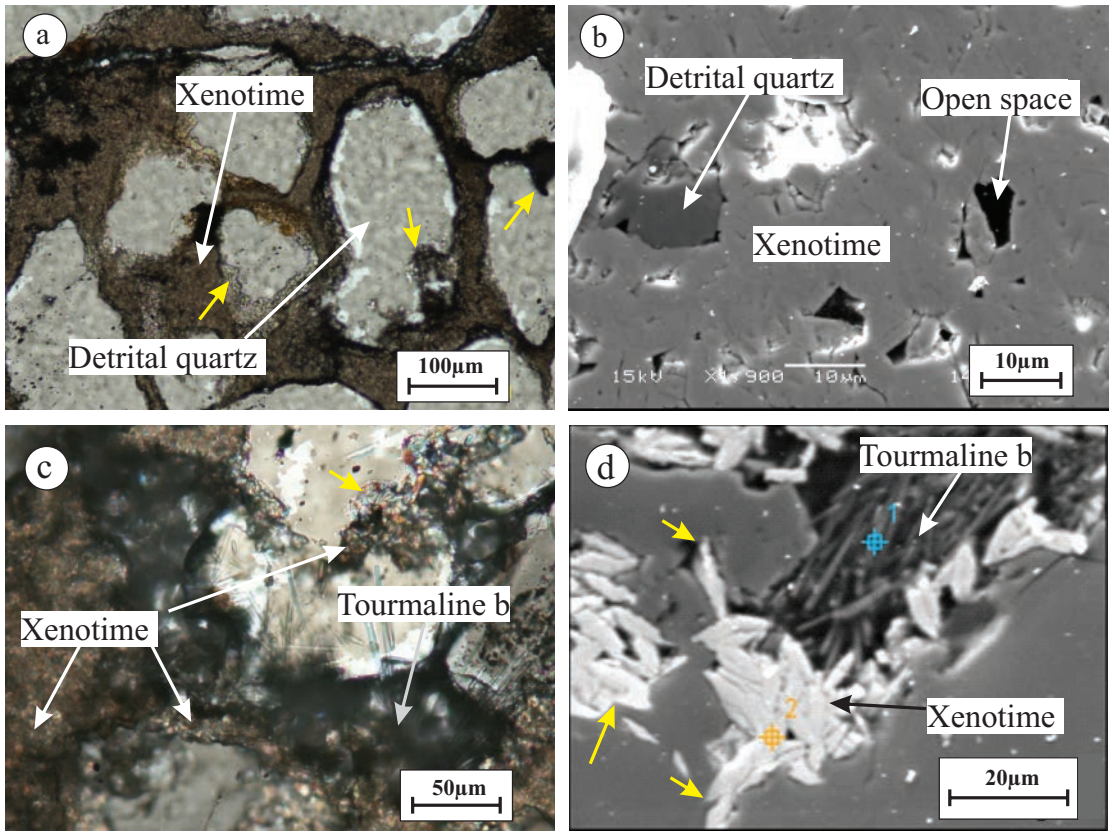

Fig. 6. Photomicrographs and SEM images showing the mode of occurrence of xenotime. (a) Fine-grained xenotime occurring in interstitial space and as a replacement of detrital quartz grains. (b) SEM image showing the detail of a massive aggregate of fine-grained, anhedral xenotime crystals. (c) Xenotime closely associated with tourmaline b. (d) SEM view of coexisting xenotime and tourmaline b crystals. Corrosion on detrital quartz grains is indicated by the yellow arrows.

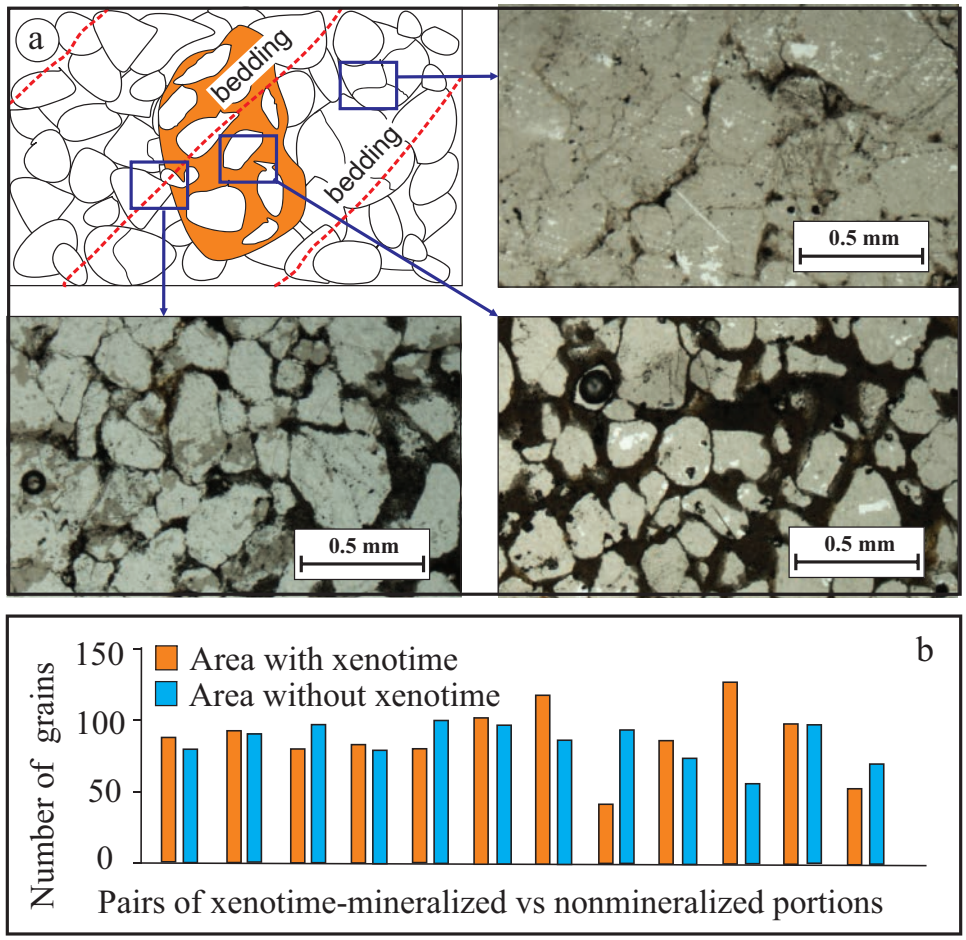

Fig. 7. (a) Sketch and photomicrographs showing the distribution of xenotime and detrital quartz grains within and outside a xenotime-rich patch. Dashed red line represents the approximate lamina in the hand sample. (b) Histogram comparing the number of detrital quartz grains within the same laminae per view area between sandstone inside and outside the xenotime-rich patch.

SIMS Oxygen Isotope Analyses of Quartz and Tourmaline

Oxygen isotopes of coprecipitated quartz and tourmaline

Four samples in which textural features suggest coprecipitation of quartz and tourmaline (Fig. 10) were selected for in situ analysis of O isotopes with SIMS, and the results are presented in Table 2. The pairs of minerals include drusy quartz phase b tourmaline (Fig. 10a, b) and hydrothermal syntaxial quartz phase a tourmaline (Fig. 10c, d). The $\delta^{18}O_{VSMOW}$ values of hydrothermal syntaxial quartz range from 13.7 to 17.7‰, and those of drusy quartz range from 15.9 to 18.9‰ (Table 2). The $\delta^{18}O_{VSMOW}$ values of phase a tourmaline range from 7.3 to 12.3‰, and those of phase b tourmaline range from 10.5 to 12.6‰ (Table 2). The analytical results of neighboring spots (for the same mineral) are consistent in some cases (e.g., Fig. 10c, d) and notably different in other cases (e.g., Fig. 10b).

Calculation of temperatures and isotopic composition of the parent fluid

The temperatures and the oxygen isotope compositions of the parent fluid from which quartz and tourmaline coprecipitated were calculated using the $1000\ln\alpha_{Quartz\text{-}Tourmaline}$ of Jiang (1998) and the $1000\ln\alpha_{Quartz\text{-}Water}$ isotope fractionation equations of Clayton et al. (1972), respectively. The equation of Jiang (1998) was chosen over that of Kotzer et al. (1993) because the former was based on a broader database. The calculated temperatures range from 89° to 385°C for the formation of the tourmaline a hydrothermal syntaxial quartz pairs and from 92° to 249°C for the formation of the tourmaline b drusy quartz pairs (Table 2, Fig. 11). There is no systematic difference in temperature between the two pairs of tourmaline and quartz (Fig. 11), and the average temperature is 185°C (Table 2). The calculated $\delta^{18}O_{VSMOW}$ values of the parent fluid range from –6.2 to +10.8‰ for the tourmaline a quartz pairs and from –3.1 to +7.3‰ for the tourmaline b quartz pairs (Table 2). No systematic difference between tourmaline a and tourmaline b was observed in $\delta^{18}O_{VSMOW}$ values (Fig. 11), and the average $\delta^{18}O_{VSMOW\text{-}fluid}$ is +1.6‰ (Table 2).

Fluid Inclusion Analysis

Fluid inclusion types and occurrences

Fluid inclusions were studied in hydrothermal syntaxial quartz and drusy quartz that occupy the same paragenetic position as xenotime mineralization. At room temperature, four types of

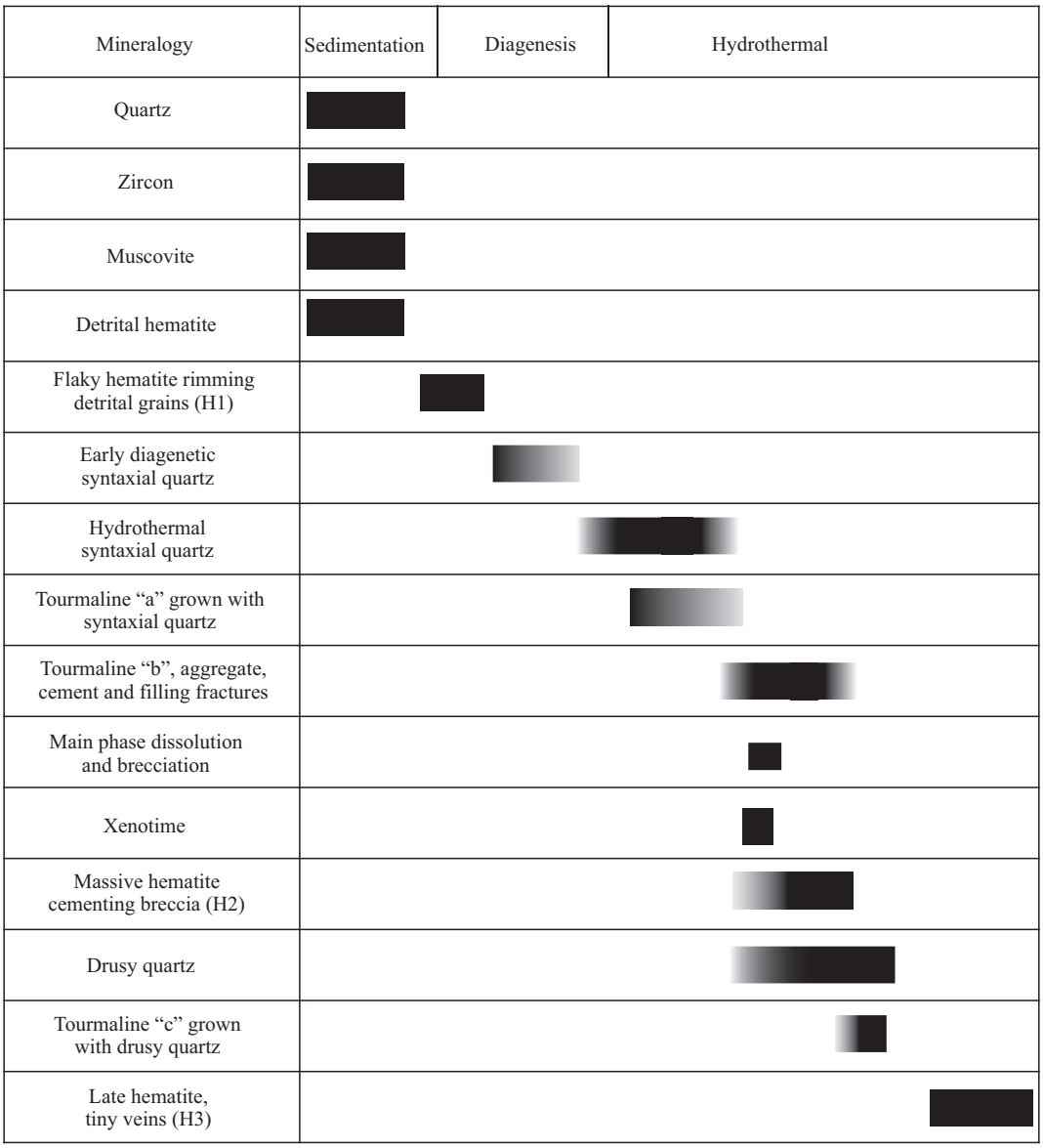

Fig. 8. Diagram illustrating the paragenetic sequence of events and mineral formation in the Maw zone REE deposit. The gradations in the fill of some of the boxes indicate a gradual phasing in and/or phasing out of that mineral growth.

fluid inclusions were identified (Fig. 12): (1) liquid-dominated biphase (liquid + vapor), (2) vapor-dominated biphase (vapor + liquid), (3) monophase (vapor only), and (4) triphase (liquid + vapor + solid).

The liquid-dominated biphase inclusions are composed of a liquid phase and a vapor phase at room temperature, and contain <50% vapor (Fig. 12a). The vapor-dominated biphase inclusions are also composed of a liquid phase and a vapor phase at room temperature, but the vapor percentage in those inclusions is >50% (Fig. 12b). The monophase inclusions are composed of only vapor at room temperature, without any visible liquid phase (Fig. 12c). The triphase inclusions consist of a liquid phase, a vapor phase, and a halite crystal (Fig. 12d). All four types of fluid inclusion were observed in hydrothermal syntaxial quartz and drusy quartz.

The fluid inclusions occur in four modes: (1) confined to individual growth zones (primary; Fig. 12f), (2) along short intracrystal healed fractures (pseudosecondary; Fig. 12e), (3) in clusters (possibly primary), and (4) isolated (possibly primary). The first three modes were treated as FIAs, and isolated fluid inclusions were treated separately. The occurrence of vapor-only and biphase inclusions with variable vapor/liquid ratios (Fig. 12f) within individual FIAs is interpreted to indicate boiling and heterogeneous trapping (i.e., entrapment of both liquid and phase within individual inclusions; Chi et al., 2017). Similarly, the occurrence of biphase and triphase inclusions within an FIA (Fig. 12g) is interpreted to indicate heterogeneous trapping (i.e., entrapment of both liquid and solid for some inclusions and only liquid for other inclusions). Furthermore, the oversaturation of NaCl before trapping is interpreted to be related to increased salinity in the liquid phase due to boiling. Note that, because of the

Table 1. SHRIMP U-Pb Isotope Analytical Data of Xenotime from the Maw Zone REE Deposit and Calculated Ages

Spot name	$^{204}Pb/^{206}Pb$	% err	$^{254}UO/^{194}Y_2O$	% err	f206^{204}	U (ppm, approx.)	Th (ppm, approx.)	$^{207}Pb/^{235}U$	% err	$^{206}Pb/^{238}U$	% err	ρ	$^{207}Pb/^{206}Pb$	% err	Ages (Ma) $^{206}Pb/^{238}U$ age	1σ	$^{207}Pb/^{206}Pb$ age	1σ
11506-001.2	5.2E-5	71	0.29	1.68	0.094	496	15	3.068	2.5	0.2322	2.1	0.8643	0.09583	1.24	1346	25	1544	23
11506-002.1	9.3E-4	28	0.13	0.70	1.489	436	12	3.300	4.5	0.2433	2.1	0.5313	0.09834	3.82	1404	26	1593	70
11506-002.2	8.7E-4	20	0.14	0.67	1.400	424	12	3.430	4.2	0.2615	3.0	0.7327	0.09513	2.86	1498	40	1531	53
11506-004.1	3.3E-4	24	0.16	0.76	0.524	473	4	3.466	2.6	0.2576	2.0	0.8111	0.09758	1.51	1478	27	1578	28
11506-005.1	5.2E-4	37	0.21	1.02	0.836	461	24	3.387	4.1	0.2560	2.3	0.6088	0.09598	3.26	1469	31	1547	60
11506-006.1	5.6E-4	42	0.14	0.69	0.900	401	6	2.972	4.4	0.2329	2.1	0.5443	0.09254	3.68	1350	25	1479	68
11506-007.1	3.3E-4	24	0.16	0.73	0.531	428	6	3.183	2.5	0.2439	2.0	0.8072	0.09463	1.50	1407	25	1521	28
11506-013.1	4.9E-5	69	0.13	0.68	0.079	395	1	3.179	2.8	0.2380	2.0	0.7689	0.09687	1.76	1376	25	1565	33
11506-016.1	2.1E-4	33	0.13	0.77	0.339	417	2	3.169	2.6	0.2426	2.1	0.8176	0.09474	1.49	1400	26	1523	28
11506-017.1	3.5E-4	28	0.19	0.71	0.557	493	5	3.018	3.2	0.2340	2.6	0.8197	0.09351	1.85	1356	32	1498	35
11506-019.1	2.8E-4	33	0.14	0.76	0.458	454	3	2.974	2.9	0.2300	2.1	0.7609	0.09377	1.89	1335	26	1504	35
11506-022.1	1.0E-4	35	0.20	2.58	0.166	477	14	3.410	2.1	0.2570	1.9	0.8959	0.09623	0.95	1475	25	1552	18
11506-023.1	7.3E-5	41	0.21	2.26	0.117	473	6	3.400	2.1	0.2542	1.9	0.9084	0.09704	0.87	1460	24	1568	16
11506-024.1	4.4E-5	60	0.18	1.15	0.071	459	12	3.367	2.2	0.2547	1.9	0.8987	0.09589	0.95	1463	25	1546	18

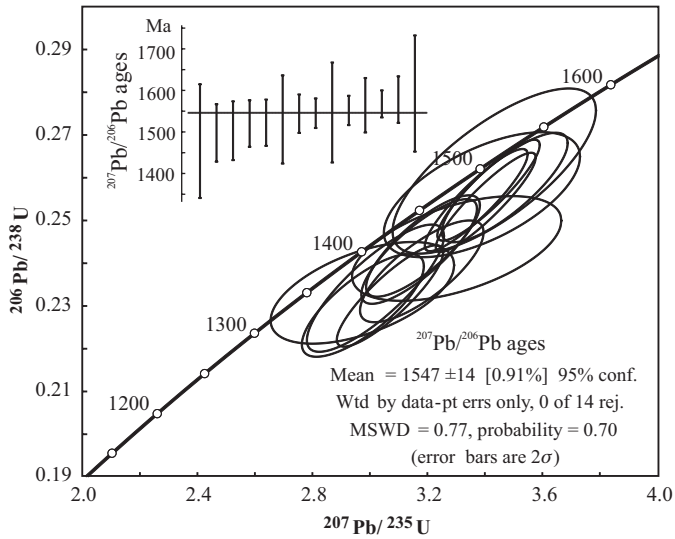

Fig. 9. A concordia diagram showing the distribution of xenotime U-Pb ages. The inset shows the $^{207}Pb/^{206}Pb$ ages and average.

low concentrations of nonaqueous volatiles (<1 mole %; see below), boiling rather than immiscibility is used to describe the coexistence of liquid and vapor in this paper.

Microthermometry

Fluid inclusions in FIAs that suggest homogeneous trapping, using the criteria of Goldstein and Reynolds (1994), were analyzed microthermometrically. For isolated fluid inclusions, the FIA criteria cannot be used, but the same concept is applied: any isolated inclusion that showed significantly different vapor/liquid ratios from those in nearby areas was not considered (Chi and Lu, 2008). The vapor-only inclusions could not be studied microthermometrically, and all the vapor-dominated inclusions, which are interpreted to have been trapped heterogeneously, were not considered either. A few triphase inclusions were measured, and they all showed halite dissolution temperatures significantly higher than those of the vapor disappearance temperatures. These triphase inclusions coexist with biphase inclusions and are interpreted to have been heterogeneously entrapped. As such, microthermometric measurements of these inclusions were not used. Only measurements obtained from microthermometry of liquid-dominated biphase inclusions were retained for detailed interpretation of data. The microthermometric data of individual fluid inclusions (including those that formed FIAs and those that consisted of isolated inclusions) are listed in Table 3. In order to avoid data bias, the mean values of individual FIAs, rather than those of individual fluid inclusions, are presented in the diagrams shown in Figures 13 to 15.

Many of the inclusions were unable to freeze even after cooling to –185°C. For those that did freeze, the first melting event took place below –50°C, but the exact first-melting temperatures could not be measured precisely. The nonfreezing behavior and low first-melting temperatures are characteristics shared by fluid inclusions of the H_2O-NaCl-$CaCl_2$ system (Davis et al., 1990; Chi et al., 2014; Chu et al., 2016). Many fluid inclusions showed ice as the last melting

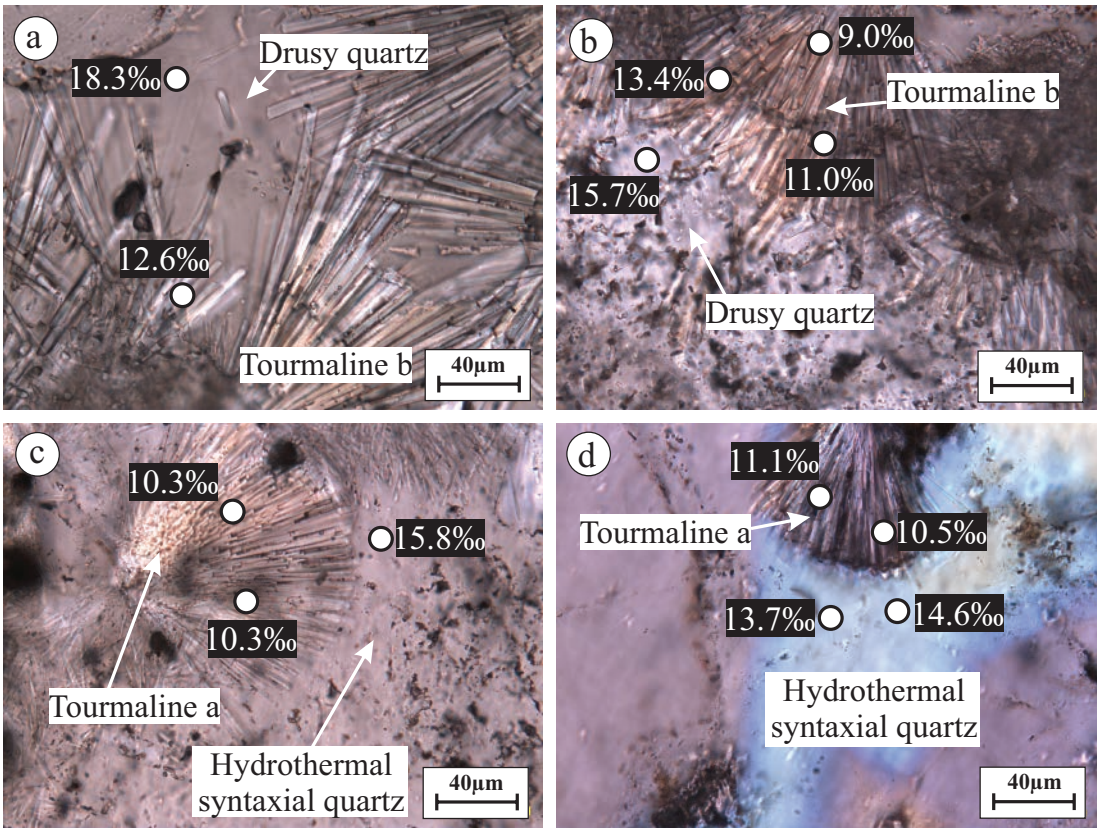

Fig. 10. Photomicrographs showing the locations of analytical spots of different pairs of tourmaline b and drusy quartz (a and b) and tourmaline a and hydrothermal syntaxial quartz (c and d) for oxygen isotopes with SIMS. The $\delta^{18}O_{VSMOW}$ values are shown beside the spots.

Table 2. Measured $\delta^{18}O$ Values of Coprecipitated Quartz and Tourmaline and Calculated Temperatures and Isotopic Compositions of the Parent Fluid

	Quartz		Tourmaline			
Sample no.	Host mineral	$\delta^{18}O_{VSMOW}$ (‰)	Host mineral	$\delta^{18}O_{VSMOW}$ (‰)	Temperature (°C) Jiang (1998)	$\delta^{18}O_{VSMOW}$ (‰)-water Clayton et al. (1972)
14-MR-44, drill hole ZQ-8-83, 40.3 m	Drusy quartz	18.9	Tourmaline b	10.5	92.9	–3.1
	Drusy quartz	18.3	Tourmaline b	12.6	178.3	5.0
	Drusy quartz	15.7	Tourmaline b	11.0	227.7	5.6
14-MR-45, drill hole ZQ-8-83, 40.8 m	Drusy quartz	19.2	Tourmaline b	10.7	91.7	–3.0
		15.9		10.5	190.7	3.5
	Hydrothermal syntaxial quartz	14.6	Tourmaline a	11.1	323.8	8.5
		13.7		10.5	351.6	8.4
	Hydrothermal syntaxial quartz	15.2	Tourmaline a	12.3	385.2	10.8
	Hydrothermal syntaxial quartz	15.4	Tourmaline a	10.2	198.8	3.5
	Hydrothermal syntaxial quartz	15.5	Tourmaline a	8.9	141.3	–0.9
14-MR-46, drill hole ZQ-8-83, 49.7 m	Hydrothermal syntaxial quartz	17.7	Tourmaline a	11.1	140.0	1.2
	Hydrothermal syntaxial quartz	15.1	Tourmaline a	7.3	108.8	–4.8
	Hydrothermal syntaxial quartz	15.8	Tourmaline a	10.3	183.3	2.9
	Hydrothermal syntaxial quartz	16.8	Tourmaline a	8.5	93.4	–5.1
14-MR-77, drill hole 85-1, 8.5 m	Hydrothermal syntaxial quartz	15.6	Tourmaline a	7.5	97.5	–5.7
	Hydrothermal syntaxial quartz	16.4	Tourmaline a	7.8	88.8	–6.2
	Drusy quartz	16.3	Tourmaline b	12.0	249.2	7.3
Average					184.9	1.6

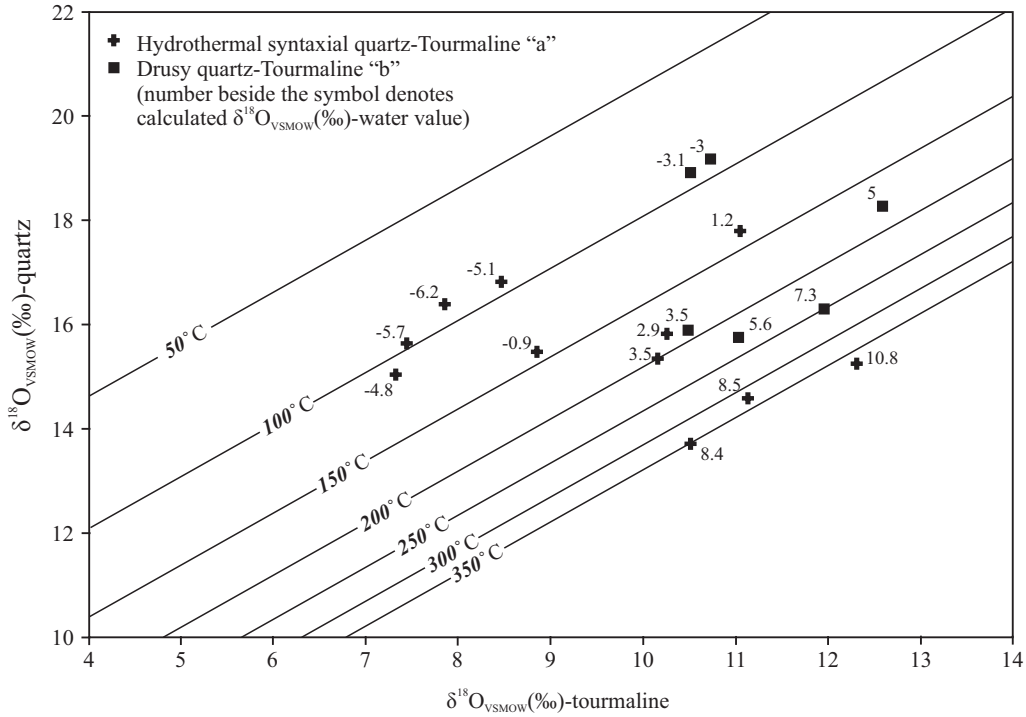

Fig. 11. Plot of measured $\delta^{18}O_{VSMOW}$ of tourmaline vs. calculated $\delta^{18}O_{VSMOW}$ of parent water. The lines delineate the equilibrium temperatures calculated using the $1000\ln\alpha_{Tourmaline\text{-}Water}$ oxygen isotope fractionation equation of Jiang (1998).

phase, and others showed hydrohalite as the last melting phase. In the former case, the hydrohalite melting temperatures could not be measured with certainty, and the ice-melting temperatures were used to calculate the salinities and maximum X_{NaCl} values. Using this approach, the results plot on the ice-hydrohalite cotectic boundary of the ternary H_2O-NaCl-$CaCl_2$ plot shown in Figure 13. Note that the actual composition of a fluid inclusion should be in the field of ice along the isotherm as shown by the arrow attached to the data point (Fig. 13); the actual X_{NaCl} values are lower than shown by the data points, but the salinities are similar to those at the data points because the isotherms are nearly parallel to the NaCl-$CaCl_2$ axis (Fig. 13). Where both ice-melting and hydrohalite-melting temperatures were measured, many of the measured hydrohalite-melting temperatures were higher than the peritectic melting temperature of hydrohalite in the H_2O-NaCl system (0.1°C; Table 3), even after numerous attempts using different heating rates, suggesting metastability. In such cases, the hydrohalite-melting temperatures could not be used to calculate fluid compositions using the program of Steele-MacInnis et al. (2011). Instead, a trial-and-error method was used to determine the maximum stable hydrohalite-melting temperature for a given ice-melting temperature, and the results plot on the hydrohalite-halite cotectic boundary of the ternary H_2O-NaCl-$CaCl_2$ plot shown in Figure 13; the actual composition of a fluid inclusion should be in the field of hydrohalite, as shown by the arrows attached to the data point, and the actual X_{NaCl} value and salinity should be slightly lower than those shown by the data point (Fig. 13). The salinities obtained using these approaches range from 11.8 to 28.3 wt % NaCl + $CaCl_2$ (with the majority being >24 wt %), and the maximum calculated X_{NaCl} values range from 0.14 to 1.0 (Table 3), suggesting the presence of both NaCl-dominated (two-thirds of the data) and $CaCl_2$-dominated (one-third of the data) brines.

The mean values of total homogenization temperatures (T_h) of individual biphase inclusions that compose FIAs range from 77° to 178°C, with an average of 124°C, and T_h values of isolated biphase inclusions range from 63° to 162°C, with an average of 112°C (Table 3; Fig. 14). With the exception of two isolated fluid inclusions that show significantly lower salinities than the rest of the dataset, the T_h and salinity data for the FIAs and isolated fluid inclusions show similar distribution patterns characterized by a narrow range of salinities and a relatively wide range of total homogenization temperatures (Fig. 15). The averages for the measured T_h and calculated salinity and X_{NaCl} are 117°C, 25.0 wt %, and 0.55, respectively.

Cryogenic Raman spectroscopic analysis

Nonaqueous volatiles were not detected in the vapor phase of any of the fluid inclusions using Raman spectroscopic analysis. Selected fluid inclusions were measured for Raman spectra at –185°C with an aim to determine the solute composition through detection of various hydrates (Dubessy et al., 1982; Samson and Walker, 2000; Ni et al., 2006; Baumgartner and Bakker, 2010; Chi et al., 2014). All the spectra showed clear peaks of hydrohalite and mixed hydrohalite and antarcticite, and some also showed shoulders next to mixed hydrohalite and antarcticite peaks that are attributed to antarcticite and other $CaCl_2$ hydrates. However, $CaCl_2$-dominated spectra were not obtained in this study.

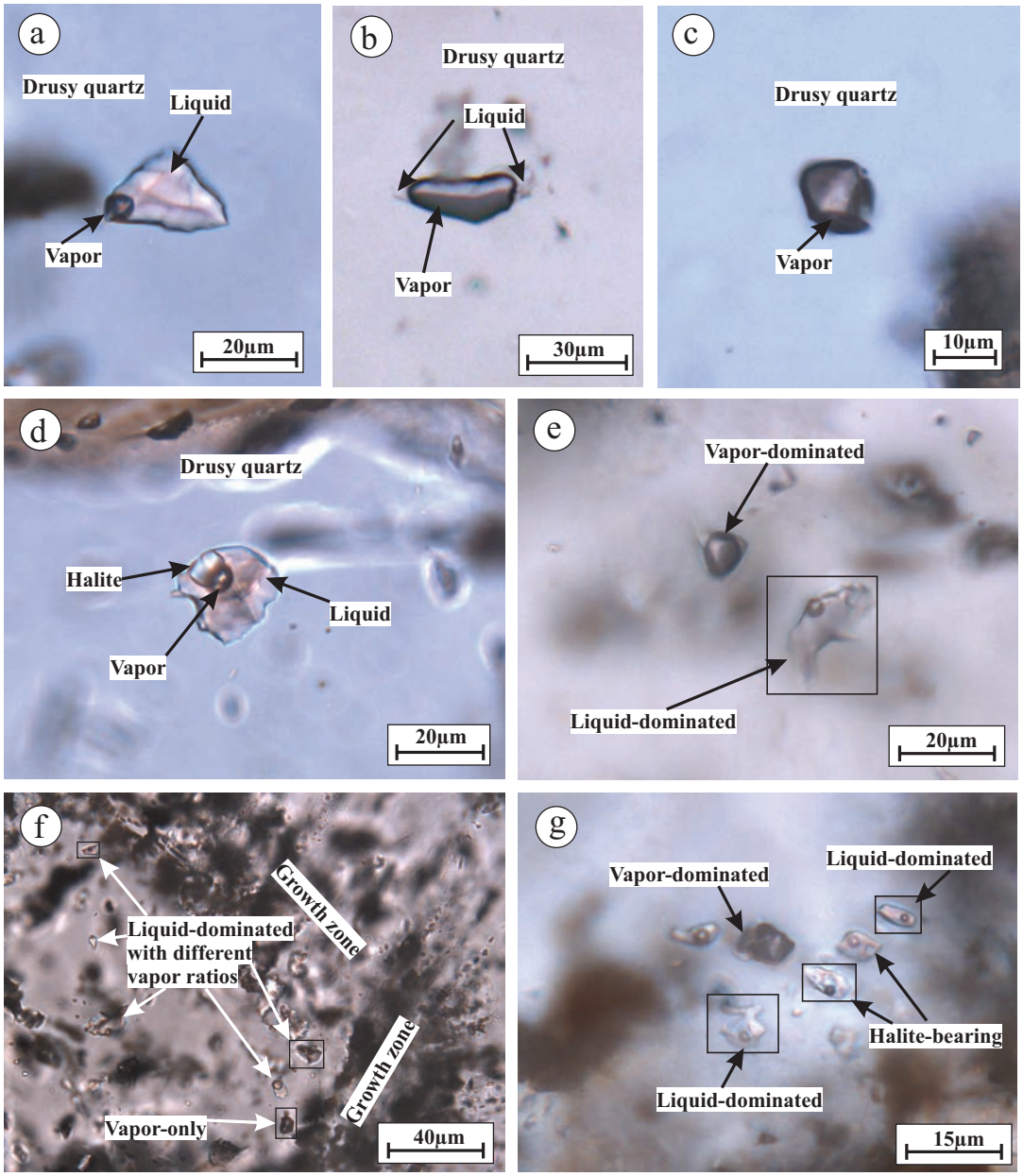

Fig. 12. Photomicrographs of different types of fluid inclusions (all in plane-polarized light). (a) A liquid-dominated biphase (liquid + vapor) inclusion in drusy quartz (sample 14-MR-047-d). (b) A vapor-dominated biphase (liquid + vapor) inclusion in drusy quartz (sample 14-MR-044). (c) Monophase (vapor-only) fluid inclusions in drusy quartz (sample 14-MR-041). (d) A three-phase (liquid + vapor + solid) inclusion in drusy quartz (sample 14-MR-047-k). (e, f) Fluid inclusions with different vapor/liquid ratios along the same growth zones (sample 14-MR-044). (g) Coexistence of liquid-dominated, vapor-dominated, and halite-bearing triphase inclusions in a cluster (sample 14-MR-10). Note that fluid inclusions enclosed in the rectangles are from different depths and were brought to focus as insets.

Bulk fluid inclusion analysis of volatiles

Five samples of separated drusy quartz were analyzed to obtain volatile compositions of bulk fluid inclusions, and the results are shown in Table 4. The data obtained from successive bursts are consistent within individual samples, and the results are similar among different samples (Table 4). H_2O is the dominant component (avg. 99.39 mole %) in all cases, and N_2 (avg. 0.44 mole %) and CO_2 (avg. 0.15 mole %) are present in subordinate proportions (Table 4). The measured concentrations of CH_4, H_2, He, Ar, and H_2S are mostly below 0.01 mole % (Table 4).

Discussion

Environment and mechanism of xenotime mineralization in the Maw zone REE deposit

Petrographic evidence indicates that the xenotime mineralization took place after significant compaction of the host rocks (Fig. 7). This is supported by the xenotime $^{207}Pb/^{206}Pb$

Table 3. Microthermometric Results of Fluid Inclusion Assemblages and Isolated Fluid Inclusions from the Maw REE Zone Deposit

Sample no.	Host mineral	Occurrences	Size (μm)	V %	T_m-ice (°C)	T_m-HH (°C)	T_h (V → L) (°C)	Salinity (wt %)	X_{NaCl} (max.)
14-MR-039, outcrop (472891-6370416)	Drusy quartz	Cluster	8	5	–37.4	-	74	28.3	0.14
			4	5	-	-	80	-	-
		Cluster	6	7	–26.1	-	92	25	0.50
			8	7	–25.5	-	88	24.8	0.54
		Cluster	8	8	-	-	104	-	-
			4	8	-	-	105	-	-
			8	8	-	-	95	-	-
		Cluster	14	10	–26.2	–4.5	128	27.6	0.55
			8	10	–34.5	-	116	27.5	0.18
		Isolated	8	10	–23.1	-	100	24.0	0.76
14-MR-010, drill hole ZQ-10-83, 46.85 m	Drusy quartz	Cluster	6	10	-	-	129	-	-
			6	10	-	-	119	-	-
		Growth zone	6	10	-	-	125	-	-
			6	10	-	-	133	-	-
		Growth zone	6	9	–33.6	-	107	27	0.20
			3	9	-	-	124	-	-
			5	9	-	-	128	-	-
		Cluster	20	7	–25.1	–5	137	26.7	0.62
			16	7	–24.9	-	119	24.6	0.59
			12	7	–25.3	-	117	24.7	0.55
		Cluster	6	5	–25.4	-	120	24.8	0.55
			4	5	–25.4	-	111	24.8	0.55
		Healed fracture	10	5	–26.1	–4.5	107	27.4	0.56
			10	5	–26.2	–4.5	108	27.4	0.55
			8	5	–24.7	–8.6	119	26.4	0.65
		Cluster	10	7	–25.5	–3.7	157	27.2	0.60
			4	7	–25.3	–3.5	152	27.1	0.61
		Cluster	16	15	-	-	134	-	-
			10	5	-	-	118	-	-
		Growth zone	14	5	–25.6	–3.8	152	27.3	0.59
			14	5	–25.6	-	146	24.8	0.53
			8	5	–26.4	-	153	25.1	0.48
			6	5	–25.4	-	152	24.7	0.55
			14	5	–25.3	–3.5	147	27.1	0.61
		Cluster	18	5	–28.9	-	151	25.9	0.35
			20	5	–29.3	–9	133	28	0.39
		Cluster	6	7	–26.5	-	132	25.1	0.47
			4	7	–26.5	-	117	25.1	0.47
			4	7	–26.9	–8.4	126	27.1	0.51
		Growth zone	14	5	-	-	181	-	-
			8	5	–34.2	-	165	27.4	0.19
		Growth zone	8	10	-	-	104	-	-
			8	10	-	-	120	-	-
			8	15	-	-	114	-	-
			6	14	-	-	109	-	-
		Cluster	8	7	–27.1	–5.5	157	27.6	0.50
			8	7	-	-	162	-	-
		Cluster	12	10	–26.4	-	183	25.1	0.48
			8	10	-	-	172	-	-
		Growth zone	10	10	–28.5	–7	120	28.0	0.43
			5	17	-	-	125	-	-
			12	12	-	-	108	-	-
			8	10	-	-	119	-	-
			10	8	-	-	114	-	-
			12	10	-	-	114	-	-
			10	12	-	-	114	-	-
			6	15	-	-	104	-	-
		Isolated	7	20	-	-	95	-	-
		Isolated	10	10	-	-	111	-	-
		Isolated	14	15	–8	-	130	11.8	1.00
		Isolated	10	10	–34.5	-	100	27.5	0.18
		Isolated	10	15	–25.1	-	124	24.6	0.57
		Isolated	10	10	-	-	123	-	-
		Isolated	20	15	–24	-	139	24.3	0.67
		Isolated	8	7	-	-	100	-	-
		Isolated	15	16	–24.7	-	121	24.5	0.60
		Isolated	6	15	-	-	128	-	-

Table 3. *(Cont.)*

Sample no.	Host mineral	Occurrences	Size (μm)	V %	T_m-ice (°C)	T_m-HH (°C)	T_h (V → L) (°C)	Salinity (wt %)	X_{NaCl} (max.)
		Isolated	8	15	–26.2	–4.5	113	27.4	0.55
		Isolated	15	20	–23.2	-	143	24.0	0.75
		Isolated	10	10	-	-	102	-	-
		Isolated	8	10	–19.4	-	162	22.0	1.00
		Isolated	12	20	-	-	142	-	-
		Isolated	8	12	–28.9	–7.5	158	28.2	0.41
		Isolated	22	20	-	-	137	-	-
		Isolated	8	18	-	-	133	-	-
		Isolated	10	10	–21.8	-	71	23.5	0.91
		Isolated	8	17	–24.9	-	123	24.6	0.59
		Isolated	11	15	-	-	118	-	-
		Isolated	6	15	–31	-	114	26.5	0.27
14-MR-047, drill hole ZQ-8-83, 53.2 m	Drusy quartz on syntaxial quartz	Cluster	6	10	-	-	98	-	-
			4	5	-	-	86	-	-
		Growth zone	26	5	–27	–5.4	127	27.2	0.50
			10	5	–26	-	136	24.9	0.50
		Cluster	20	8	–23.8	–1.9	125	26.6	0.73
			20	10	–23.7	–1.8	124	26.8	0.74
			8	8	–25.3	–3.5	107	27.2	0.61
		Healed fracture	8	7	-	-	129	-	-
			4	10	-	-	123	-	-
			6	7	-	-	133	-	-
		Cluster	4	5	-	-	128	-	-
			6	5	-	-	127	-	-
			6	5	-	-	108	-	-
		Isolated	10	10	-	-	102	-	-
		Isolated	28	15	-	-	117	-	-
		Isolated	6	15	–23.9	–2	105	26.8	0.72
		Isolated	6	15	-	-	113	-	-
		Isolated	16	10	–25	–3.2	126	27.0	0.63
		Isolated	8	5	-	-	98	-	-
		Isolated	8	10	–27.1	-	100	25.3	0.44
		Isolated	8	12	-	-	63	-	-
14-MR-029, drill hole ZQ-10-83, 217.9 m	Drusy quartz	Isolated	10	5	-	-	74	-	-
		Isolated	8	8	–27.1	-	102	25.3	0.44
		Isolated	10	10	–25.9	-	119	24.9	0.51
		Isolated	10	11	–25.8	-	95	24.9	0.52
		Isolated	10	10	–10.4	-	138	14.3	1.00
		Isolated	8	10	–21.8	-	71	23.5	0.91
		Isolated	7	8	–24	-	96	24.3	0.67
		Isolated	8	9	–26.4	-	81	25.1	0.48
Average							117	25.0	0.55

Notes: V % = vapor percentage, T_m-ice = ice-melting temperature, T_m-HH = hydrohalite-dissolution temperature, T_h = homogenization temperature, X_{NaCl} (max.) = maximum NaCl/(NaCl + $CaCl_2$) weight ratio, – = data unavailable

age of 1547 ± 14 Ma (Fig. 9), which is much younger than the host rocks (>1644 Ma, the age of the Wolverine Point Formation above the Manitou Falls Formation, which hosts the deposit). Therefore, the xenotime mineralization in the Maw zone did not take place during early diagenesis, a conclusion also supported by the homogenization temperatures of fluid inclusions (Table 3; Fig. 14) and fluid temperature estimated from the quartz-tourmaline oxygen isotope geothermometer (Table 2; Fig. 11). The mineralization is considered to be of hydrothermal nature, in the sense that either the mineralizing fluid was hot or the fluid was hotter than the burial temperature of the host rocks (Machel and Lonnee, 2002). In order to clarify the last point, a discussion regarding the pressure and depth as well as temperature conditions that attended the mineralization is provided below.

The coexistence of vapor-dominated and liquid-dominated fluid inclusions, as described above, suggests that the hydrothermal fluid responsible for mineralization reached a point of vapor saturation. In such a case, the total homogenization temperature of the liquid-rich biphase fluid inclusions would be indicative of the trapping temperature and the fluid pressure at this temperature would represent the trapping pressure (P_h). Using the empirical equation of state of Bodnar (1993) for the system of H_2O-NaCl included in the FLUIDS program of Bakker (2003), the vapor-saturated fluid pressures calculated for total homogenization temperatures from 60° to 178°C and salinities from 25 to 28 wt % are less than 8 bars. The P_h values thus obtained would be underestimated if nonaqueous volatiles were present in sufficient amounts. However, the bulk fluid inclusion analyses presented above

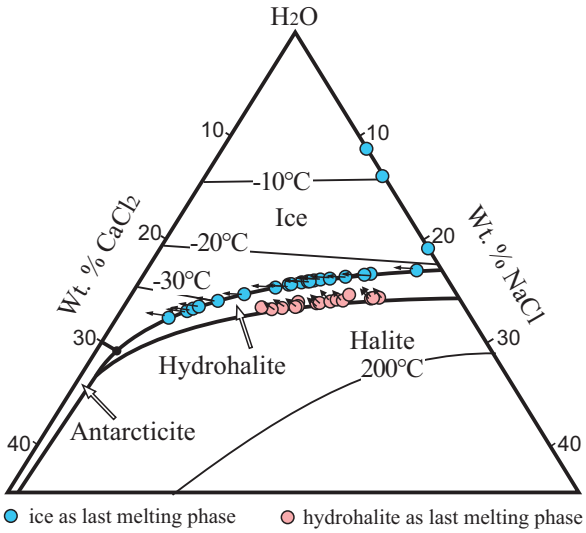

Fig. 13. H_2O-NaCl-$CaCl_2$ phase diagram showing the composition of the fluid inclusions from the Maw zone REE deposit. Circles with light blue color represent the inclusions with ice as the last melting phase, and circles with pink color represent inclusions with hydrohalite as the last melting phase. Note that the arrows attached to the blue data points indicate that the actual compositions of the fluid inclusions lie on the isotherms in the field of ice in the direction pointed by the arrows; the arrows attached to the pink data points indicate that the actual compositions of the fluid inclusions lie in the field of hydrohalite in the direction pointed by the arrows.

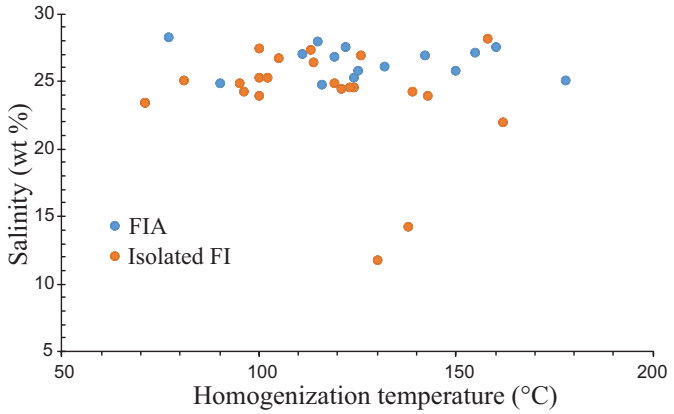

Fig. 15. Salinity-total homogenization temperature diagram from FIAs and isolated fluid inclusions from the Maw zone deposit.

indicate that nonaqueous volatiles represent less than 1 mole % of the total of the volatiles (Table 4), and even if the presence of 1 mole % of CO_2 is assumed, the P_h values calculated using the equations of state of Duan et al. (1992a, b, 1996) for the H_2O-CO_2 system are less than 17 bars. These low-pressure values likely do not represent the ambient fluid pressure, but rather reflect conditions at the instant when boiling took place. The fluid was likely in the liquid state most of the time, rather than at the liquid-vapor phase boundary, and the fluid pressure was higher than the P_h values discussed above.

Based on regional stratigraphy, the thickness of the strata between the host rocks (the Manitou Falls Formation) and that having similar ages as the xenotime mineralization (the Douglas Formation, with an Re-Os age of 1541 Ma; Creaser and Stasiuk, 2007) is less than 1.5 km (Ramaekers et al., 2007) and, therefore, the depth of mineralization was possibly less than 2.5 km (using a maximum decompaction factor of 1.7, as assumed in Chi et al., 2013). Furthermore, considering the sand-dominated nature of the Athabasca Basin, the fluid pressure regime was likely near hydrostatic (Chi et al., 2013). Therefore, the ambient fluid pressure during mineralization in the Maw zone was possibly less than 250 bars.

The fluid temperatures estimated from fluid inclusion and isotopic thermometry are significantly higher than the ambient burial temperature (possibly <100°C for a depth of <2.5 km). Thus, the mineralization environment is epithermal in nature, as has been proposed for uranium mineralization in the region (Chi and Chu, 2016; Chu and Chi, 2016; Chi et al., 2017; Liang et al., 2017). The high fluid temperatures in a shallow basinal environment also imply that the fluids, which may have been originally derived from the basin (although contribution of original basement fluids cannot be excluded), circulated deeply into the basement, became hot, and ascended back into the basin, as proposed by Bons et al. (2014) for unconformity-related ore deposits. However, the exact depth of fluid penetration into the basement required to account for the high temperatures depends on the thermal gradient, which in turn depends on whether or not there were anomalous heat sources at depth. The fluid pressure may have fluctuated between hydrostatic (a few hundred bars, when the fluid was in the liquid state) and subhydrostatic (a few tens of bars), probably following episodic events of hydraulic

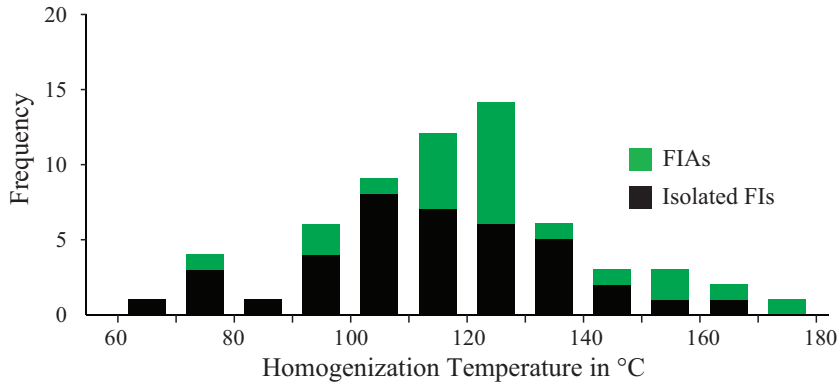

Fig. 14. Histogram of homogenization temperatures of FIAs and isolated fluid inclusions from the Maw zone deposit.

Table 4. Bulk Fluid Volatile Compositions of Inclusions (mole %) in Drusy Quartz from the Maw Zone REE Deposit

H_2O	CO_2	CH_4	N_2	H_2	H_2S	He	Ar
Sample 15-MR-90, drill hole ZQ-10-83, drusy quartz							
99.21	0.03	0.00	0.74	0.01	0.00	0.00	0.01
99.76	0.03	0.01	0.19	0.00	0.00	0.00	0.00
99.39	0.07	0.01	0.52	0.00	0.00	0.00	0.01
99.82	0.04	0.00	0.13	0.00	0.00	0.00	0.00
99.77	0.13	0.01	0.06	0.03	0.00	0.00	0.00
99.69	0.11	0.01	0.16	0.02	0.00	0.00	0.00
Sample 14-MR-12, drill hole ZQ-10-83, 221.15 m, drusy quartz							
97.58	1.24	0.00	1.15	0.01	0.00	0.00	0.01
99.48	0.10	0.00	0.41	0.00	0.00	0.00	0.01
99.28	0.60	0.00	0.10	0.02	0.00	0.00	0.00
99.87	0.10	0.00	0.03	0.00	0.00	0.00	0.00
99.80	0.10	0.00	0.09	0.01	0.00	0.00	0.00
99.38	0.42	0.00	0.20	0.00	0.00	0.00	0.00
99.19	0.37	0.00	0.43	0.00	0.00	0.00	0.01
99.88	0.04	0.00	0.08	0.00	0.00	0.00	0.00
99.90	0.04	0.00	0.06	0.00	0.00	0.00	0.00
99.89	0.08	0.00	0.03	0.00	0.00	0.00	0.00
Sample 14-MR-13, drill hole ZQ-10-83, 227.18 m, drusy quartz							
99.79	0.03	0.01	0.16	0.00	0.00	0.00	0.00
99.79	0.06	0.01	0.14	0.00	0.00	0.00	0.00
99.82	0.03	0.00	0.14	0.00	0.00	0.00	0.00
99.88	0.03	0.01	0.08	0.00	0.00	0.00	0.00
99.89	0.03	0.01	0.08	0.00	0.00	0.00	0.00
99.84	0.09	0.01	0.07	0.00	0.00	0.00	0.00
99.87	0.07	0.01	0.05	0.00	0.00	0.00	0.00
99.86	0.10	0.02	0.03	0.00	0.00	0.00	0.00
Sample 14-MR-56, drill hole ZQ-9-83, 248.3 m, drusy quartz							
99.50	0.08	0.00	0.41	0.00	0.00	0.00	0.01
99.69	0.09	0.00	0.22	0.00	0.00	0.00	0.00
99.54	0.03	0.00	0.42	0.00	0.00	0.00	0.01
99.58	0.05	0.00	0.36	0.00	0.00	0.00	0.01
99.68	0.04	0.00	0.26	0.00	0.00	0.00	0.00
99.78	0.04	0.01	0.18	0.00	0.00	0.00	0.00
99.78	0.08	0.00	0.14	0.00	0.00	0.00	0.00
99.80	0.06	0.00	0.13	0.00	0.00	0.00	0.00
Sample 14-MR-57, drill hole ZQ-9-83, 237 m, drusy quarrtz							
95.69	0.68	0.08	3.48	0.02	0.00	0.00	0.05
97.98	0.26	0.05	1.68	0.01	0.00	0.00	0.03
99.05	0.14	0.01	0.76	0.01	0.00	0.00	0.01
98.53	0.14	0.01	1.28	0.01	0.00	0.00	0.02
99.45	0.07	0.00	0.46	0.01	0.00	0.00	0.01
98.54	0.17	0.01	1.24	0.02	0.00	0.00	0.02
99.09	0.12	0.01	0.76	0.01	0.00	0.00	0.01
99.14	0.14	0.02	0.66	0.03	0.00	0.00	0.01
Average							
99.39	0.15	0.01	0.44	0.01	0.00	0.00	0.01

fracturing and seismic pumping (Sibson, 1987; Sibson et al., 1988). The abrupt fluid pressure drop during fracturing may have been responsible for the boiling as recorded by fluid inclusions, similar to the earthquake-induced "flash vaporization" model proposed by Weatherley and Henley (2013) for fault-controlled quartz-vein gold mineralization. Fluids from different sources were drawn to the breccia pipe and mixed, causing xenotime precipitation and silicification, hematitization, and tourmalinization.

Because the solubility of REE phosphates is very low in hydrothermal fluids (Williams-Jones et al., 2012; Williams-Jones, 2015; Migdisov et al., 2016), it is highly unlikely that significant amounts of phosphorus can be transported with REEs by the same fluid. Rather, two separate fluids, one rich in P and the other rich in REEs, were involved in the mineralization; alternatively, the REE-rich fluid may have reacted with P-rich minerals (such as apatite and crandallite) to precipitate xenotime. The former mechanism is supported by the occurrence of xenotime with tourmaline and drusy quartz as open-space filling (Fig. 6c, d), and the latter is suggested by the texture showing xenotime replacing sandstone (Fig. 6a). Quirt et al. (1991) proposed that the P-bearing fluid was a basinal brine within the Athabasca Basin, based on empirical and experimental observations that phosphorus mobility was possible in basinal fluids in equilibrium with illite and kaolinite, and that diagenetic apatite and crandallite were developed in the Athabasca Basin. Regarding the sources of the REEs, Quirt et al. (1991) thought they were extracted from detrital zircon grains in the Athabasca Basin, though they also recognized garnet in the basement as a potential source. While we agree with Quirt et al. (1991) on the basinal source for P, we are more inclined to a basement source (garnet) for the REEs, for reasons discussed below.

Although zircon can be an important carrier of REEs, the relative proportions of Y + HREEs (from Eu to Lu) vary widely, especially for detrital zircon grains in sedimentary basins (Hoskin and Schaltegger, 2003) and, therefore, REEs extracted from zircon cannot readily explain the high Y + HREE enrichment at Maw zone. Similarly, monazite may not be the main source of Y and HREEs at Maw zone, as monazite is light REE (LREE) enriched and there are no other LREE-enriched minerals (such as APS minerals) associated with the xenotime to account for the depletion of LREEs in the latter, as was proposed for uraninite from the unconformity-related uranium deposits (Mercadier et al., 2011). In contrast, garnet is known to be an important carrier of Y and HREEs in the Earth's crust and mantle, and garnets grown during upper amphibolite facies metamorphism of pelites (rich mainly in the almandine end-member) have been reported to contain from 7 to 7,000 ppm Y + HREEs (with a median value of 313 ppm), with the Y + HREEs representing >99% of the total REEs (Bea, 1996; Bea et al., 1997; Yang et al., 1999; Pyle et al., 2001; Corrie and Kohn, 2008). Although the exact lithologies of the basement directly below Maw zone have not been documented, exploratory work done in the vicinity indicates that the basement rocks in the area are composed of variably garnetiferous and graphitic pelitic gneiss and quartzite of the Daly Lake Group, as part of the Wollaston Supergroup (Yeo and Delaney, 2007; Card, 2013; Card and Noll, 2016). Garnet (almandine) is unstable at low pressures and at temperatures

below ~550° to 650°C in the presence of excess water (Spear, 1993), and pervasive alteration of garnet by fluid circulating in the basement could release large amounts of Y and HREEs. The comparatively much less abundant and much more insoluble monazite and xenotime (Migdisov et al., 2009; Williams-Jones et al., 2012; Migdisov and Williams-Jones, 2014; Williams-Jones, 2015; Migdisov et al., 2016) and, to a lesser extent, zircon (Linnen et al., 2014, and references therein), contained in the pelitic gneiss, would not have contributed significant LREEs to the fluid at temperatures <250°C. Furthermore, the epithermal nature of the mineralization, as discussed above, necessitates that the mineralizing fluid ascended from depth in the basement, in order to account for the relatively high fluid temperature for a shallow mineralization environment. The calculated $\delta^{18}O$ values of the parent fluids of tourmaline and quartz from Maw zone (Table 2; Fig. 11) are generally compatible with a basement source, although they are also comparable to those of basinal fluids in the Athabasca Basin (Richard et al., 2013; Cuney and Kyser, 2015).

Therefore, we propose that a basinal fluid circulated deeply into the basement, became heated and mixed with fluids already in the basement, reacted with garnetiferous lithologies and extracted Y and HREEs, ascended to a shallow depth, and mixed with a P-rich basinal fluid (and reacted with local P-rich minerals) to form the Maw zone deposit. The Y and HREEs were most likely transported as Cl complexes (Migdisov et al., 2016), given the high salinities documented by fluid inclusions. The redox state and the relationship between the REE-rich fluid and basinal fluids as well as those involved in the unconformity-related uranium deposits are further discussed in the next section.

Relationships between REE mineralization at Maw zone and unconformity-related uranium deposits in the region

The Maw zone REE mineralization and regional unconformity-related uranium deposits were proposed to be genetically related, based on their similarities in petrography and geochemistry of the alteration zones (MacDougall, 1990; Quirt et al., 1991; Hanly, 2001). This hypothesis is consistent with the new data collected in this study. Detailed petrographic work demonstrates that the xenotime mineralization at Maw zone occupies the same paragenetic position as tourmaline, which has the same composition (i.e., alkali-deficient Mg tourmaline, or magnesiofoitite) as that closely associated with unconformity-related uranium mineralization in the area (e.g., the Phoenix and McArthur River uranium deposits, Fig. 1; O'Connell et al., 2015; Adlakha and Hattori, 2016; Wang, 2016). The xenotime $^{207}Pb/^{206}Pb$ age (1547 ± 14 Ma) is also consistent with that of uranium mineralization in the region. Although a basin-scale primary uranium mineralization event was proposed at ca. 1590 Ma (Alexandre et al., 2009), the maximum uraninite U-Pb ages and/or muscovite Ar-Ar ages obtained from the largest unconformity-related uranium deposits in the eastern part of the Athabasca basin are mostly ≤ ca. 1540 Ma (e.g., Fayek et al., 2002; Cloutier et al., 2009, 2011). Although $CaCl_2$-dominated Raman spectra were not obtained in this study, the microthermometric data (Table 3; Fig. 13) clearly demonstrate the presence of $CaCl_2$-dominated fluid. The development of both Na-rich and Ca-rich brines and the range of T_h and salinity of fluid inclusions from the Maw zone deposit (Table 3; Figs. 13–15) are strikingly similar to those reported from unconformity-related uranium deposits (Derome et al., 2005; Richard et al., 2016; Wang, 2016). However, it should be noted that the low concentrations (undetectable with Raman spectroscopy) of radiolytic (H_2, O_2) and other trace gases (CO_2, CH_4, C_2H_6, N_2) in the fluid inclusions from Maw zone are different from the common occurrence of these gases (detectable with Raman) in fluid inclusions from unconformity-related uranium deposits (Richard, 2017).

The key question to be addressed is, if the Maw zone REE mineralization is genetically related to the unconformity-related uranium deposits, why there is no uranium enrichment in the former. A seemingly straightforward answer would be that the mineralizing fluid for Maw zone was similar to that for the unconformity-related uranium deposits, and the lack of uranium mineralization at Maw zone is due to the lack of reducing agents to precipitate uraninite. A similar mechanism was proposed by Cloutier et al. (2010) for the Zone K alteration system in the Wheeler River area, where the lack of uranium mineralization was interpreted to be due to the lack of uraniferous fluid at the moment of arrival of the reducing fluid. Pan et al. (2013) suggested that the mineralizing fluid for Maw zone is different from the oxidizing uranium-carrying basinal fluid related to the unconformity-related uranium deposits, because the lack of radiation-induced damage in the different generations of quartz at Maw zone indicates that the fluids were low in uranium. The low concentration of uranium in the Maw zone ore fluid is also reflected by the low concentrations of the so-called radiolytic gases (H_2 and O_2) in the fluid inclusions (Table 4), in contrast to those found in the uranium deposits (Richard, 2017). Three scenarios that can link the REE mineralizing fluids at Maw zone with the unconformity-related uranium deposits and explain the low uranium concentration in the fluid are discussed below (Fig. 16).

In a first scenario (Fig. 16a), as proposed by Hanly and Hagni (2002), the REEs of the Maw zone deposit were derived from remobilization of the REEs contained in preexisting uranium mineralization (Fig. 16a, time 1). According to Cuney and Kyser (2015), REEs and radiogenic Pb can be mobilized during alteration of uranium oxides under reducing conditions, where uranium remains essentially immobile (Fig. 16a, time 2). This mechanism may explain the absence of uranium and overwhelming predominance of HREEs with respect to LREEs in the Maw zone REE deposit, as the uraninite in the unconformity-related uranium deposits is also enriched in HREEs and Y (Fayek and Kyser, 1997; Jefferson et al., 2007; Mercadier et al., 2011; Normand, 2014). However, this model implies that the REE mineralization at Maw zone postdates the unconformity-related uranium mineralization, which is inconsistent with the inference of contemporaneousness of the two mineralizing systems based on paragenesis.

In a second scenario (Fig. 16b), the mineralizing fluid for Maw zone was originally similar to the ore-forming fluid of the unconformity-related uranium deposits, containing high concentrations of U and REEs. The uranium may have been stripped off the fluid following its circulation through basement rocks that comprise reducing lithologies or mixing with a

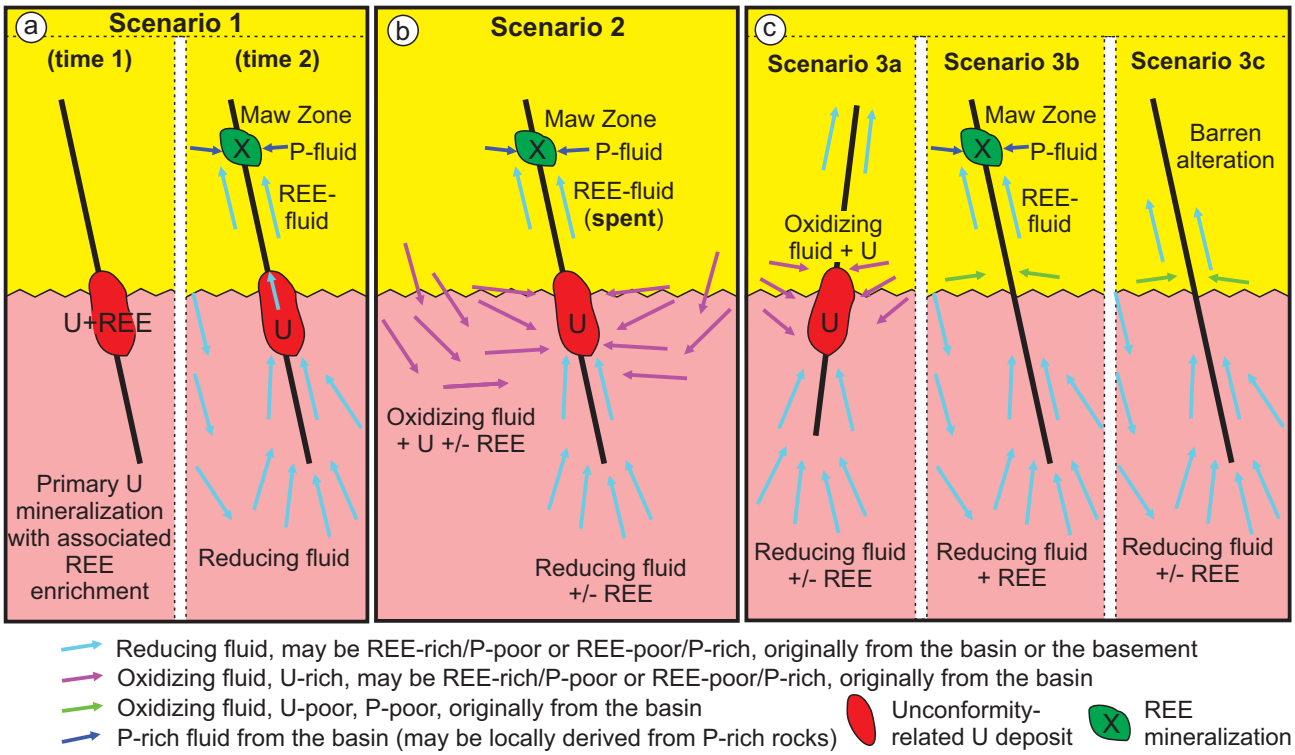

Fig. 16. Schematic model illustrating three scenarios of relationships between REE mineralization and unconformity-related uranium mineralization in the Athabasca Basin. See text for detailed explanation.

reducing fluid (Fig. 16b), thereby causing a dramatic decrease in oxygen fugacity (Komninou and Sverjensky, 1996) and the formation of unconformity-related uranium deposits. The reduced spent fluid could still have the capacity to carry large amounts of REEs, boron, and ferrous iron, given the high fluid salinities favorable for REE transport (Williams-Jones et al., 2012; Williams-Jones, 2015). However, this model has the difficulty of explaining why the spent fluid was still enriched in HREEs and Y relative to LREEs after deposition of large amounts of uraninite, which is also enriched in HREEs.

A third scenario (Fig. 16c) is that the ore-forming fluid for Maw zone represents one of the fluids involved in the formation of the unconformity-related uranium deposits—a fluid rich in reducing agents, boron, and REEs, but poor in phosphorus (the other fluid being oxidizing and U rich). When this fluid encountered an oxidizing, uranium-bearing fluid, uranium mineralization took place (Fig. 16c, scenario 3a), and APS minerals (which are commonly found in unconformity-related uranium deposits; Gaboreau et al., 2007; Cloutier et al., 2010; Adlakha and Hattori, 2015) were precipitated if the uranium-bearing fluid also contained phosphorus (note that, although uranium can be transported as phosphate complexes, as summarized in Kyser and Cuney, 2009, and Cuney and Kyser, 2015, the high salinities and low pH values of the Athabasca basinal fluids favor Cl as the major ligand for uranium transport; Richard et al., 2012). Conversely, when the reducing fluid did not encounter uranium-bearing fluid, but rather a phosphorus-rich basinal fluid, as in the case of the Maw zone deposit (scenario 3b), only REE mineralization took place. Although little is known about the distribution of the phosphorus-rich fluid, its presence in the Athabasca Basin is indicated by the development of diagenetic apatite and crandallite (Quirt et al., 1991; Davis et al., 2008). Phosphorus-rich minerals in the sandstones may have also contributed to xenotime precipitation through fluid-rock reactions. If the reducing fluid did not encounter either uranium- or phosphorus-rich fluids or lithologies, then no uranium deposits or xenotime deposits were developed (Fig. 16c, scenario 3c). The reducing fluid is responsible for tourmaline alteration, regardless of whether it encountered uranium-bearing or uranium-poor fluid, thus explaining the common occurrence of tourmaline with similar composition and paragenetic position at Maw zone and the unconformity-related uranium deposits. This model is similar to the one proposed by Cloutier et al. (2010) for the uranium-barren Zone K in the Wheeler River area, in which uranium-bearing basinal fluids passed through the sandstones of the Manitou Falls Formation in the early hydrothermal stage, prior to the arrival of a reducing fluid ascending from the basement, thus precluding uranium precipitation. It is notable that the average $\delta^{18}O_{VSMOW}$ value estimated for the reducing fluid in Zone K (+2.5‰; Cloutier et al., 2010) is similar to that which we obtained for the Maw zone mineralizing fluids (+1.6‰; Table 2), although we have a wider data range (Table 2; Fig. 11). Furthermore, given the low concentrations of CH_4 and H_2S detected by mass spectrometric analysis of bulk fluid inclusions in this study, we suggest that the most important reducing agent, in the case of the Maw zone mineralizing fluid, may be dissolved Fe^{2+} rather than reducing gases. The oxidation of Fe^{2+} during mineralization may be responsible for the hematitization commonly found in the uranium deposits as well as the Maw zone REE deposit.

The third scenario is particularly attractive, considering the development of a regional-scale alteration (including tourmaline) corridor in the southeastern Athabasca Basin encompassing several major uranium deposits (Earle and Sopuck, 1989; Fig. 1). The alteration corridor is much larger than the uranium deposits themselves, and is dominantly barren, either of U or of REEs. This implies that uranium-rich fluid and phophorus-rich fluid were not widespread in the Athabasca Basin, at least not at the time of the uprising of the reducing fluid causing the regional alteration. A similar inference was made based on geochemical and mass balance studies of the ubiquitous bleaching phenomena in the Athabasca Basin, which indicate introduction of reducing fluids without accompanying uranium mineralization (Chu et al., 2015). Thus, unlike the conventional uranium mineralization model that assumes the general availability of uranium-bearing oxidizing fluids in the Athabasca Basin and uses the availability of reducing agents (lithologies or fluids) as the determining factor for uranium mineralization, the discussion above draws attention to the limited distribution of uranium-bearing fluids (for uranium mineralization) and phosphorus-bearing fluid (for REE mineralization).

Based on the potential genetic relationships between REE and uranium mineralization, as discussed above, and given the numerous occurrences of uranium mineralization in the Athabasca Basin, there is the potential to find more hydrothermal REE mineralization similar to that present at Maw zone. Major reactivated basement structures that controlled the formation of unconformity-related uranium deposits may also be used as conduits of REE-carrying hydrothermal fluids, which have the potential to form REE deposits if encountering phosphorus-bearing fluids. On the other hand, hydrothermal REE mineralization and associated alteration in the shallower parts of the basin may be used as an indicator of reducing hydrothermal fluids rising from the basement (although the ultimate source of the fluid was likely from the basin, as has been extensively shown by halogen and noble gas analyses of fluid inclusions; Richard et al., 2011, 2014; Leisen et al., 2012), which have the potential to form uranium deposits near the unconformity, depending on the availability of uranium-bearing fluids.

Conclusions

Based on field, petrographic, geochronological, O isotope, and fluid inclusion studies, the following conclusions are made regarding the formation of the Maw zone REE deposit and its relationship with unconformity-related uranium deposits:

1. Xenotime was formed after significant compaction of the host rocks, rather than during early diagenesis. The age of the mineralization is 1547 ± 14 Ma, which is much younger than the host rocks (>1644 Ma), and is comparable to the primary mineralization age for unconformity-related uranium deposits in the eastern part of the Athabasca Basin.
2. The xenotime mineralization took place in an epithermal environment. The depth of mineralization is inferred to be less than 2.5 km based on regional stratigraphy, and the temperature of the mineralizing fluids is inferred to have been ~180°C based on fluid inclusion microthermometric data and paired quartz-tourmaline oxygen isotope data. Fluid pressure may have fluctuated between hydrostatic and subhydrostatic regimes, and boiling took place when fluid pressure episodically and abruptly dropped below hydrostatic values, probably related to episodic faulting and brecciation.
3. The mineralizing fluids are characterized by Na-rich and Ca-rich brines, which are similar to those documented for the unconformity-related uranium deposits. This, together with the observation that the tourmaline associated with the xenotime in the Maw zone and that associated with unconformity-related uranium deposits nearby are paragenetically and compositionally (magnesiofoetite) similar, as well as their similarity in mineralization ages, suggests that the REE mineralization and uranium mineralization are related to similar hydrothermal systems.
4. The ore-forming fluid for the Maw zone REE deposit was rich in Y and HREEs, boron, and ferrous iron, but poor in uranium. It may represent the reducing fluid causing uraninite precipitation in the unconformity-related uranium deposits. Xenotime mineralization resulted from mixing between this fluid and a P-rich (and U-poor) fluid from the basin, as well as reaction between the REE-bearing fluid and a P-rich lithology. The absence of uranium mineralization at Maw zone is due to lack of U-rich fluid rather than lack of reducing agents.

Acknowledgments

This study is supported by a grant from the Saskatchewan Geological Survey (to Chi) and NSERC-Discovery grants (to Normand and Chi). We would like to thank Denison Mines for accommodation during our fieldwork, and Zenghua Li, Kewen Wang, Ken Ashton, Clark Gamelin, and Yongxing Liu for assistance and helpful discussion in field work and core examination. Eric Potter is thanked for reviewing an early draft of the manuscript. Ryan Sharpe is thanked for his assistance in SIMS analysis of O isotopes, and Tom Pestaj is thanked for assistance in the GSC SHRIMP laboratory. The detailed reviews by Antonin Richard and Jonathan Cloutier greatly improved the paper.

REFERENCES

Adlakha, E.E., and Hattori, K., 2015, Compositional variation and timing of aluminum phosphate-sulfate minerals in the basement rocks along the P2 fault and in association with the McArthur River uranium deposit, Athabasca Basin, Saskatchewan, Canada: American Mineralogist, v. 100, p. 1386–1399.

——2016, Paragenesis and composition of tourmaline types along the P2 fault and McArthur River uranium deposit, Athabasca Basin, Canada: Canadian Mineralogist, v. 54, p. 661–679.

Alexandre, P., Kyser, K., Thomas, D., Polito, P., and Marlat, J., 2009, Geochronology of unconformity-related uranium deposits in the Athabasca Basin, Saskatchewan, Canada and their integration in the evolution of the basin: Mineralium Deposita, v. 44, p. 41–59.

Annesley, I.R., Madore, C., Shi, R., and Krogh, T.E., 1997, U-Pb geochronology of thermotectonic events in the Wollaston Lake area, Wollaston Domain: A summary of 1994–1996 results: Saskatchewan Geological Survey, Saskatchewan Energy and Mines, Miscellaneous Report 97–4, p. 162–173.

Bakker, R.J., 2003, Package FLUIDS 1. Computer programs for analysis of fluid inclusion data and for modeling bulk fluid properties: Chemical Geology, v. 194, p. 3–23.

Barker, M., 2007, Structural analysis of the Maw zone: A sub-economic REE deposit: B.Sc. thesis, Antigonish, St. Francis Xavier University, 82 p.

Baumgartner, M., and Bakker, R.J., 2010, Raman spectra of ice and salt hydrates in synthetic fluid inclusions: Chemical Geology, v. 275, p. 58–66.

Bea, F., 1996, Residence of REE, Y, Th and U in granites and crustal protoliths: Implications for the chemistry of crustal melts: Journal of Petrology, v. 37, p. 521–552.

Bea, F., Montero, P., Garuti, G., and Zacharini, F., 1997, Pressure-dependence of rare earth element distribution in amphibolite- and granulite-grade garnets. A LA-ICP-MS study: Geostandards Newsletter, v. 21, p. 253–270.

Blamey, N.J.F., 2012, Composition and evolution of crustal, geothermal and hydrothermal fluids interpreted using quantitative fluid inclusion gas analysis: Journal of Geochemical Exploration, v. 116–117, p. 17–27.

Bodnar, R.J., 1993, Revised equation and table for determining the freezing point depression of H_2O-NaCl solutions: Geochimica et Cosmochimica Acta, v. 57, p. 683–684.

Bons, P.D., Fusswinkel, T., Gomez-Rivas, E., Markl, G., Wagner, T., and Walter, B., 2014, Fluid mixing from below in unconformity-related ore deposits: Geology, v. 42, p. 1035–1038.

Bosman, S.A., Card, C.D., MacKnight, S.G., and Boulanger, S., 2012, The Athabasca Basin ore systems project: An update on geochemistry, spatial data, and core logging: Saskatchewan Geological Survey, Miscellaneous Report 4.2, Paper A-5, 10 p.

Card, C.D., 2012, A proposed domainal reclassification for Saskatchewan's Hearne and Rae provinces: Saskatchewan Geological Survey, Saskatchewan Ministry of the Economy, Miscellaneous Report 2012-4.2, Paper A-11, 9 p.

——2013, Altered pelitic gneisses and associated "quartzite ridges" beneath the southeastern Athabasca Basin: Alteration facies and their relationship to uranium deposits along the Wollaston-Mudjatik transition: Saskatchewan Geological Survey, Saskatchewan Ministry of the Economy, Miscellaneous Report 2013-4.2, Paper A-4, 23 p.

Card, C.D., and Noll, J., 2016, Host-rock protoliths, pre-ore metasomatic mineral assemblages and textures, and exotic rocks in the western Athabasca Basin: Ore-system controls and implications for the unconformity-related uranium model: Saskatchewan Geological Survey, Saskatchewan Ministry of the Economy, Miscellaneous Report 2016-4.2, Paper A-8, 19 p.

Card, C.D., Pana, D., Portella, P., Thomas, D.J., and Annesley, I.R., 2007, Basement rocks of the Athabasca Basin, Saskatchewan, and Alberta: Geological Survey of Canada Bulletin 588, p. 69–87.

Chen, S., Hattori, K., and Grunsky, E.C., 2016, Multivariate statistical analysis of the REE-mineralization of the Maw zone, Athabasca Basin, Canada: Journal of Geochemical Exploration, v. 161, p. 98–111.

Chi, G., and Chu, H., 2016, Unconformity-related uranium mineralization in the Athabasca Basin, Canada: Deep burial diagenetic-hydrothermal or epithermal? [abs.]: European Association of Geochemistry and of the Geochemical Society, Goldschmidt 2016 Conference, Yokohama, Japan, June 26–July 1, 2016, Abstract Volume, p. 475.

Chi, G., and Lu, H., 2008, Validation and representation of fluid inclusion microthermometric data using the fluid inclusion assemblage (FIA) concept: Acta Petrologica Sinica, v. 9, p. 1945–1953.

Chi, G., Bosman, S.A., and Card, C.D., 2013, Numerical modeling of fluid pressure regime in the Athabasca basin and implications for fluid flow models related to the unconformity-type uranium mineralization: Journal of Geochemical Exploration, v. 125, p. 8–19.

Chi, G., Chu, H., Scott, R., and Chou, I.M., 2014, A new method for determining fluid compositions in the H_2O-NaCl-$CaCl_2$ system with cryogenic Raman spectroscopy: Acta Geologica Sinica, v. 88, p. 1169–1182.

Chi, G., Haid, T., Quirt, D., Fayek, M., Blamey, N.J.F., and Chu, H., 2017, Petrography, fluid inclusion analysis, and geochronology of the End uranium deposit, Kiggavik, Nunavut, Canada: Mineralium Deposita, v. 52, p. 211–232.

Chu, H., and Chi, G., 2016, Thermal profiles inferred from fluid inclusion and illite geothermometry from sandstones of the Athabasca basin: Implications for fluid flow and unconformity-related uranium mineralization: Ore Geology Reviews, v. 75, p. 284–303.

Chu, H., Chi, G., Bosman, S., and Card, C., 2015, Diagenetic and geochemical studies of sandstones from drill core DV10-001 in the Athabasca basin, Canada, and implications for uranium mineralization: Journal of Geochemical Exploration, v. 148, p. 206–230.

Chu, H., Chi, G., and Chou, I.-M., 2016, Freezing and melting behaviors of H_2O-NaCl-$CaCl_2$ solutions in fused silica capillaries and glass-sandwiched films: Implications for fluid inclusion studies: Geofluids, v. 16, p. 518–532.

Clayton, R.N., O'Neil, J.R., and Mayeda, T.K., 1972, Oxygen isotope exchange between quartz and water: Journal of Geophysical Research, v. 77, p. 3057–3067.

Cloutier, J., Kyser, K., Olivo, G.R., Alexandre, P., and Halaburda, J., 2009, The Millennium uranium deposit, Athabasca basin, Saskatchewan, Canada: An atypical basement-hosted unconformity-related uranium deposit: Economic Geology, v. 104, p. 815–840.

Cloutier, J., Kyser, K., Olivo, G.R., and Alexandre, P., 2010, Contrasting patterns of alteration at the Wheeler River area, Athabasca Basin, Saskatchewan, Canada: Insights into the apparently uranium-barren Zone K alteration system: Economic Geology, v. 105, p. 303–324.

Cloutier, J., Kyser, K., Olivo, G.R., and Brisban, D., 2011, Geochemical, isotopic, and geochronologic constraints on the formation of the Eagle Point basement-hosted uranium deposit, Athabasca Basin, Saskatchewan, Canada and recent remobilization of primary uraninite in secondary structures: Mineralium Deposita, v. 46, p. 35–56.

Corrie, S.L., and Kohn, M.J., 2008, Trace-element distributions in silicates during prograde metamorphic reactions: Implications for monazite formation: Journal of Metamorphic Geology, v. 26, p. 451–464.

Creaser, R.A., and Stasiuk, L.D., 2007, Depositional age of the Douglas Formation, northern Saskatchewan, determined by Re-Os geochronology: Geological Survey of Canada Bulletin 588, p. 341–346.

Cuney, M., and Kyser, K., 2015, Geology and geochemistry of uranium and thorium deposits: Mineralogical Association of Canada, Short Course Series, v. 46, 345 p.

Davis, D.W., Lowenstein, T.K., and Spencer, R.J., 1990, Melting behavior of fluid inclusions in laboratory-crystalized halite crystals in the systems NaCl-H_2O, NaCl-KCl-H_2O, NaCl $MgCl_2$-H_2O, and NaCl-$CaCl_2$-H_2O: Geochimica et Cosmochimica Acta, v. 54, p. 591–601.

Davis, W.J., Rainbird, R.R., Gall, Q., and Jefferson, C.J., 2008, In situ U-Pb dating of diagenetic apatite and xenotime: Paleofluid flow history within the Thelon, Athabasca and Hornby Bay basins: Geochimica et Cosmochimica Acta, v. 72, p. A203.

Derome, D., Cathelineau, M., Cuney, M., Fabre, C., Lhomme, T., and Banks, D., 2005, Mixing of sodic and calcic brines and uranium deposition at McArthur River, Saskatchewan, Canada: A Raman and laser-induced breakdown spectroscopic study of fluid inclusions: Economic Geology, v. 100, p. 1529–1545.

Duan, Z., Møller, N., and Weare, J.H., 1992a, An equation of state for the CH_4-CO_2-H_2O system: I. Pure systems from 0 to 1000 °C and 0 to 8000 bar: Geochimica et Cosmochimica Acta, v. 56, p. 2605–2617.

——1992b, An equation of state for the CH_4-CO_2-H_2O system: II. Mixtures from 50 to 1000 °C and 0 to 1000 bar: Geochimica et Cosmochimica Acta, v. 56, p. 2619–2631.

——1996, Prediction of the solubility of H_2S in NaCl aqueous solutions: An equation of state approach: Chemical Geology, v. 130, p. 15–20.

Dubessy, J., Audeoud, D., Wilkins, R., and Kosztolanyi, C., 1982, The use of the Raman microprobe MOLE in the determination of the electrolytes dissolved in the aqueous phase of fluid inclusions: Chemical Geology, v. 37, p. 137–150.

Earle, S., and Sopuck, V., 1989, Regional lithogeochemistry of the eastern part of the Athabasca Basin uranium province: International Atomic Energy Agency, Technical Document 500, p. 263–296.

England, G.L., Rasmussen, B., McNaughton, N.J., Fletcher, I.R., Groves, D.I., and Krapez, B., 2001, SHRIMP U ± Pb ages of diagenetic and hydrothermal xenotime from the Archaean Witwatersrand Supergroup of South Africa: Terra Nova, v. 13, p. 360–367.

Fayek, M., 1996, Fluid events associated with gold, uranium, and REE deposits in the Proterozoic of northern Saskatchewan, Canada: Ph.D. thesis, Saskatoon, Canada, University of Saskatchewan, 219 p.

——2013, Uranium ore deposits: A review: Mineral Association of Canada Short Course, v. 43, p. 121–147.

Fayek, M., and Kyser, T.K., 1997, Characterization of multiple fluid-flow events and rare earth element mobility associated with formation of unconformity-type uranium deposits in the Athabasca Basin, Saskatchewan: Canadian Mineralogist, v. 35, p. 627–658.

Fayek, M., Kyser, T.K., and Riciputi, L., 2002, U and Pb isotope analysis of uranium minerals by ion microprobe and the geochronology of the McArthur River and Sue Zone uranium deposits, Saskatchewan, Canada: Canadian Mineralogist, v. 40, p. 1553–1569.

Fletcher, I.R., Rasmussen, B., and McNaughton, N.J., 2000, SHRIMP U-Pb geochronology of authigenic xenotime and its potential for dating sedimentary basins: Australian Journal of Earth Sciences, v. 47, p. 845–859.

Fletcher, I.R., McNaughton, N.J., Aleinikoff, J.A., Rasmussen, B., and Kamo, S.L., 2004, Improved calibration procedures and new standards for U-Pb and Th-Pb dating of Phanerozoic xenotime by ion microprobe: Chemical Geology, v. 209, p. 209–314.

Fletcher, I.R., McNaughton, N.J., Davis, W.J., and Rasmussen, B., 2010, Matrix effects and calibration limitations in ion probe U-Pb and Th-Pb dating of monazite: Chemical Geology, v. 270, p. 31–44.

Gaboreau, S., Cuney, M., Quirt, D., Beaufort, D., Patrier, P., and Mathieu, R., 2007, Significance of aluminum phosphate-sulfate minerals associated with U unconformity-type deposits: The Athabasca Basin, Canada: American Mineralogist, v. 92, p. 267–280.

Goldstein, R.H., and Reynolds, T.J., 1994, Systematics of fluid inclusions in diagenetic minerals: Society for Sedimentary Geology (SEPM) Short Course, v. 31, p. 199.

Hanly, A.J., 2001, The mineralogy, petrology and rare earth element geochemistry of the Maw zone, Athabasca Basin, Canada: M.Sc. thesis, Rolla, Missouri, University of Missouri, 168 p.

Hanly, A.J., and Hagni, R.D., 2002, The petrology and rare earth element geochemistry of the Maw zone: An yttrium and heavy rare earth element enriched zone in the Athabasca Basin, Canada [abs.]: Geological Association of Canada, Mineralogical Association of Canada, GAC-MAC Annual Meeting, Saskatoon, 2002, Abstracts, v. 27, p. 45.

Harper, C.T., 1987, Rare earth elements and their occurrence in northern Saskatchewan: Summary of Investigations, Saskatchewan Geological Survey, Miscellaneous Report 87.4, p. 82–86.

Hitzman, M.W., and Valenta, R.K., 2005, Uranium in iron oxide-copper-gold (IOCG) systems: Economic Geology, v. 100, p. 1657–1661.

Hoatson, D.M., Jaireth, S., and Miezitis, Y., 2011, The major rare-earth-element deposits of Australia: Geological setting, exploration, and resources: Canberra, Department of Resources, Energy and Tourism, Geosience Australia, 207 p.

Hoeve, J., and Quirt, D.H., 1984, Mineralization and host rock alteration in relation to clay mineral diagenesis and evolution of the Middle-Proterozoic Athabasca Basin, northern Saskatchewan, Canada: Saskatchewan Research Council Technical Report, v. 187, 187 p.

Hoeve, J., and Sibbald, T., 1978, On the genesis of Rabbit Lake and other unconformity-type uranium deposits in northern Saskatchewan, Canada: Economic Geology, v. 73, p. 1450–1473.

Hoffman, P., 1988, United plates of America, the birth of a craton: Early Proterozoic assembly and growth of Laurentia: Annual Reviews of Earth and Planetary Sciences, v. 16, p. 543–603.

Hoskin, P.W.O., and Schaltegger, U., 2003, The composition of zircon and igneous and metamorphic petrogenesis: Reviews in Mineralogy and Geochemistry, v. 53, p. 27–62.

Jefferson, C.W., Thomas, D.J., Gandhi, S.S., Ramaekers, P., Delaney, G., Brisbin, D., Cutts, C., Portella, P., and Olson, R.A., 2007, Unconformity associated uranium deposits of the Athabasca Basin, Saskatchewan and Alberta: Geological Survey of Canada Bulletin 588, p. 273–305.

Jiang, S.Y., 1998, Stable and radiogenic isotope studies of tourmaline: An overview: Journal of the Czech Geological Society, v. 43, p. 75–90.

Kerr, W., 2010, The discovery of the Phoenix deposit: A new high-grade, Athabasca Basin unconformity-type uranium deposit, Saskatchewan, Canada: Society of Economic Geologists, Special Publication, no. 15, p. 703–728.

Knox, A., 1986, Results of the 1985 drilling program on the MAW zone and yttrium resource calculation, Wheeler River property, northern Saskatchewan: Union Oil Company of Canada Ltd., Unpublished report, 60 p.

Komninou, A., and Sverjensky, D., 1996, Geochemical modeling of the formation of an unconformity-type uranium deposit: Economic Geology, v. 91, p. 590–606.

Kositcin, N., McNaughton, N.J., Griffin, B.J., Fletcher, I.R., Groves, D.I., and Rasmussen, B., 2003, Textural and geochemical discrimination between xenotime of different origin in the Archaean Witwatersrand Basin, South Africa: Geochimica et Cosmochimica Acta, v. 67, p. 709–731.

Kotzer, T.G., and Kyser, T.K., 1995, Petrogenesis of the Proterozoic Athabasca Basin, northern Saskatchewan, Canada, and its relation to diagenesis, hydrothermal uranium mineralization and paleohydrogeology: Chemical Geology, v. 120, p. 45–89.

Kotzer, T.G., Kyser, T.K., King, R.W., and Kerrich, R., 1993, An empirical oxygen and hydrogen isotope geothermometer for quartz-tourmaline and tourmaline-water: Geochimica et Cosmochimica Acta, v. 57, p. 3421–3426.

Kyser, T.K., and Cuney, M., 2009, Unconformity-related uranium deposits: Mineralogical Association of Canada Short Course, v. 39, p. 161–220.

Kyser, K., Hiatt, E., Renac, C., Durocher, K., Holk, G., and Deckart, K., 2000, Diagenetic fluids in Paleo- and Mesoproterozoic sedimentary basins and their implications for long protracted fluid histories: Mineralogical Association of Canada Short Course Series, v. 28, p. 225–262.

Lan, Z.W., Chen, Z.Q., Li, X.H., Li, B., and Adams, D., 2013, Hydrothermal origin of the Paleoproterozoic xenotime from the King Leopold sandstone of the Kimberley Group, Kimberley, NW Australia: Implications for a ca. 1.7 Ga far-field hydrothermal event: Australian Journal of Earth Sciences, v. 60, p. 497–508.

LeCheminant, A.N., and Heaman, L.M., 1989, Mackenzie igneous events, Canada: Middle Proterozoic hotspot magmatism associated with ocean opening: Earth and Planetary Science Letters, v. 96, p. 38–48.

Leisen, M., Boiron, M.C., Richard, A., and Dubessy, J., 2012, Determination of Cl and Br concentrations in individual fluid inclusions by combining microthermometry and LAICPMS analysis: Implications for the origin of salinity in crustal fluids: Chemical Geology, v. 330–331, p. 197–206.

Li, Z., Bethune, K.M., Chi, G., Bosman, S.A., and Card, C.D., 2015, Topographic features of the sub-Athabasca Group unconformity surface in the southeastern Athabasca Basin and their relationship to uranium ore deposits: Canadian Journal of Earth Sciences, v. 52, p. 903–920.

Liang, R., Chi, G., Ashton, K., Blamey, N., and Fayek, M., 2017, Fluid compositions and P-T conditions of vein-type uranium mineralization in the Beaverlodge uranium district, northern Saskatchewan, Canada: Ore Geology Reviews, v. 80, p. 460–483.

Linnen, R.L., Samson, I.M., Williams-Jones, A.E., and Chakhmouradian, A.R., 2014, Geochemistry of the rare-earth element, Nb, Ta, Hf, and Zr deposits, *in* Scott, S.D., ed., Treatise on Geochemistry, 2nd edition, v. 13, Geochemistry of mineral deposits: Oxford, Elsevier, p. 543–568.

Long, K.R., Van Gosen, B.S., Foley, N.K., and Cordier, D., 2010, The principal rare earth elements deposits of the United States—a summary of domestic deposits and a global perspective: USGS Scientific Investigations, Report 2010–5220, 96 p.

Ludwig, K., 2009, SQUID 2: A user's manual, rev. 12: Berkeley Geochronology Center, Special Publication 5, 110 p.

MacDougall, D.G., 1990, Rare earth element mineralization in the Athabasca Group—Maw zone: Saskatchewan Geological Survey, Miscellaneous Report 90.4, p. 103–105.

Machel, H.G., and Lonnee, J., 2002, Hydrothermal dolomite—a product of poor definition and imagination: Sedimentary Geology, v. 152, p. 163–171.

McNaughton, N.J., Rasmussen, B., and Fletcher, I.R., 1999, SHRIMP uranium-lead dating of diagenetic xenotime in siliciclastic sedimentary rocks: Science, v. 285, 78–80.

Mercadier, J., Cuney, M., Lach, P., Boiron, M.-C., Bonhoure, J., Richard, A., Leisen, M., and Kister, P., 2011, Origin of uranium deposits revealed by their rare earth element signature: Terra Nova, v. 23, p. 264–269.

Migdisov, A.A., and Williams-Jones, A.E., 2014, Hydrothermal transport and deposition of the rare earth elements by fluorine-bearing aqueous liquids: Mineralium Deposita, v. 49, p. 987–997.

Migdisov, A.A., Williams-Jones, A.E., and Wagner, T., 2009, An experimental study of the solubility and speciation of the rare earth elements (III) in fluoride- and chloride-bearing aqueous solutions at temperatures up to 300°C: Geochimica et Cosmochimica Acta, v. 73, p. 7087–7109.

Migdisov, A., Williams-Jones, A.E., Brugger, J., and Caporuscio, F.A., 2016, Hydrothermal transport, deposition, and fractionation of the REE: Experimental data and thermodynamic calculations: Chemical Geology, v. 439, p. 13–42.

Ni, P., Ding, J., and Rao, B., 2006, In situ cryogenic Raman spectroscopic studies on the synthetic fluid inclusions in the systems H_2O and NaCl-H_2O: Chinese Science Bulletin, v. 51, p. 108–114.

Norman, D.I., and Moore, J.N., 2003, Organic species in geothermal waters in light of fluid inclusion gas analyses: Stanford University, 28th Workshop on Geothermal Reservoir Engineering, Stanford, California, January 27–29, 2003, p. 96–103.

Normand, C., 2014, Rare earths in Saskatchewan: Mineralization types, settings, and distributions: Saskatchewan Ministry of the Economy, Saskatchewan Geological Survey, Report 264, 105 p.

O'Connell, I., Hattori, K., Chen, S., Adlakha, E.E., and Sorba, C., 2015, Characterization of tourmaline from the Maw zone, Gryphon zone, and sandstones above the Phoenix uranium deposits, Athabasca Basin, Saskatchewan: Geological Survey of Canada, Scientific Presentation 37, Poster, doi: 10.4095/296916.

Orrell, S.E., Bickford, M.E., and Lewry, J.F., 1999, Crustal evolution and age of thermotectonic reworking in the western hinterland of Trans-Hudson Orogen, northern Saskatchewan: Precambrian Research, v. 95, p. 187–223.

Pagel, M., Poty, B., and Sheppard, M.F.S., 1980, Contribution to some Saskatchewan uranium deposits mainly from fluid inclusion and isotopic data,

in Ferguson, J., and Goleby, A., eds., Uranium in the Pine Creek Geosyncline: Vienna, International Atomic Energy Agency, p. 639–645.

Pan, Y., Yeo, G., Rogers, B., Austman, C., and Hu, B., 2013, Application of radiation induced defects in quartz to exploration for uranium deposits: A case study of the Maw zone, Athabasca Basin, Saskatchewan: Exploration and Mining Geology, v. 21, p. 115–128.

Pyle, J.M., Spear, F.S., Rudnick, R.L., and McDonough, W.F., 2001, Monazite-xenotime-garnet equilibrium in metapelites and a new monazite-garnet thermometer: Journal of Petrology, v. 42, p. 2083–2017.

Quirt, D., Kotzer, T., and Kyser, T.K., 1991, Tourmaline, phosphate minerals, zircon and pitchblende in the Athabasca Group: Maw zone and McArthur River areas: Saskatchewan Geological Survey, Report 91.4, p. 181–191.

Rainbird, R.H., Stern, R.A., Rayner, N., and Jefferson, C.W., 2007, Age, provenance, and regional correlation of the Athabasca Group, Saskatchewan and Alberta, constrained by igneous and detrital zircon geochronology: Geological Survey of Canada Bulletin 588, p. 193–209.

Ramaekers, P., Jefferson, C.W., Yeo, G.M., Collier, B., Long, D.G.F., Catuneanu, O., Bernier, S., Kupsch, B., Post, R., Drever, G., McHardy, S., Jiricka, D., Cutts, C., and Wheatley, K., 2007, Revised geological map and stratigraphy of the Athabasca Group, Saskatchewan and Alberta: Geological Survey of Canada Bulletin 588, p. 155–192.

Rasmussen, B., 1996, Early-diagenetic REE-phosphate minerals (florencite, gorceixite, crandallite and xenotime) in marine sandstones: A major sink for oceanic phosphorus: American Journal of Science, v. 296, p. 601–632.

——2005, Radiometric dating of sedimentary rocks: The application of diagenetic xenotime geochronology: Earth Science Reviews, v. 68, p. 197–243.

Richard, A., 2017, Radiolytic (H_2, O_2) and other trace gases (CO_2, CH_4, C_2H_6, N_2) in fluid inclusions from unconformity-related U deposits: Procedia Earth and Planetary Science, v. 17, p. 273–276.

Richard, A., Banks, D.A., Mercadier, J., Boiron, M.-C., Cuney, M., and Cathelineau, M., 2011, An evaporated seawater origin for the ore-forming brines in unconformity-related uranium deposits (Athabasca Basin, Canada): Cl/Br and δ^{37}Cl study of fluid inclusions: Geochimica et Cosmochimica Acta, v. 75, p. 2792–2810.

Richard, A., Rozsypal, C., Mercadier, J., Banks, D.A., Cuney, M., Boiron, M.C., and Cathelineau, M., 2012, Giant uranium deposits formed from exceptionally uranium-rich acidic brines: Nature Geoscience, v. 5, p. 142–146.

Richard, A., Boulvais, P., Mercadier, J., Cathelineau, M., Boiron, M.C., Cuney, M., and France-Lanord, C., 2013, From evaporated seawater to uranium-mineralizing brines: Isotopic and trace element study of quartz-dolomite veins in the Athabasca system: Geochimica et Cosmochimica Acta, v. 113, p. 38–59.

Richard, A., Kendrick, M.A., and Cathelineau, M., 2014, Noble gases (Ar, Kr, Xe) and halogens (Cl, Br, I) in fluid inclusions from the Athabasca Basin (Canada): Implications for unconformity-related U deposits: Precambrian Research, v. 247, p. 110–125.

Richard, A., Cathelineau, M., Boiron, M.-C., Mercadier, J., Banks, D.A., and Cuney, M., 2016, Metal-rich fluid inclusions provide new insights into unconformity-related U deposits (Athabasca Basin and basement, Canada): Mineralium Deposita, v. 51, p. 249–270.

Samson, I.M., and Walker, R.T., 2000, Cryogenic Raman spectroscopic studies in the system NaCl-$CaCl_2$-H_2O and implications for low temperature phase behavior in aqueous fluid inclusions: Canadian Mineralogist, v. 38, p. 35–43.

Sibson, R.H., 1987, Earthquake rupturing as a mineralizing agent in hydrothermal systems: Geology, v. 15, p. 701–704.

Sibson, R.H., Robert, F., and Poulsen, K.H., 1988, High angle reverse faults, fluid pressure cycling, and mesothermal gold-quartz deposits: Geology, v. 16, p. 551–555.

Spear, F.S., 1993, Metamorphic phase equilibria and pressure-temperature-time-paths: Mineralogical Society of America Monograph, 2nd printing with corrections, 1995, 799 p.

Stacey, J.S., and Kramers, J.D., 1975, Approximation of terrestrial lead isotope evolution by a two stage model: Earth and Planetary Science Letters, v. 26, p. 207–221.

Steele-MacInnis, M., Bodnar, R.J., and Naden, J., 2011, Numerical model to determine the composition of H_2O-NaCl-$CaCl_2$ fluid inclusions based on microthermometric and microanalytical data: Geochimica et Cosmochimica Acta, v. 75, p. 21–40.

Stern, R.A., and Rayner, N.R., 2003, Ages of several xenotime megacrysts by ID-TIMS: Potential reference materials for ion microprobe U-Pb geochronology: Geological Survey of Canada, Radiogenic Age and Isotopic Studies, Report 16, Current Research F1, 7 p.

Thomas, D.J., Matthews, R.B., and Sopuck, V., 2000, Athabasca Basin (Canada) unconformity-type uranium deposits: Exploration model, current mine developments and exploration directions: Geological Society of Nevada, Symposium, Geology and Ore Deposits 2000: The Great Basin and Beyond, Reno, Nevada, May 15–18, 2000, Proceedings, v. 1, p. 103–126.

Vallini, D., Rasmussen, B., Krapez, B., Fletcher, I.R., and McNaughton N.J., 2002, Obtaining diagenetic ages from metamorphosed sedimentary rocks: U-Pb dating of unusually coarse xenotime cement in phosphatic sandstone: Geology, v. 30, p. 1083–1086.

Vallini, D.A., Groves, D.I., McNaughton, N.J., and Fletcher, I.R., 2007, Uraniferous diagenetic xenotime in northern Australia and its relationship to unconformity associated uranium mineralisation: Mineralium Deposita, v. 42, p. 51–64.

Wang, K., 2016, A study of petrography, fluid inclusions and graphite alteration of the Phoenix uranium deposit, Athabasca Basin, northern Saskatchewan, Canada: Unpublished M.Sc. thesis, Regina, Saskatchewan, University of Regina, 122 p.

Weatherley, D.K., and Henley, R.W., 2013, Flash vaporization during earthquakes evidenced by gold deposits: Nature Geoscience, v. 6, p. 294–298.

Williams-Jones, A.E., 2015, The hydrothermal mobility of the rare earth elements: Ministry of Energy and Mines, British Columbia Geological Survey, Symposium on Strategic and Critical Materials Proceedings, Victoria, British Columbia, November 13–14, 2015, Paper 2015-3, p. 119–123.

Williams-Jones, A.E., Migdisov, A.A., and Samson, I.M., 2012, Hydrothermal mobilisation of the rare earth elements—a tale of "ceria" and "yttria": Elements, v. 8, p. 355–360.

Yang, P., Rivers, T., and Jackson, S., 1999, Crystal-chemical and thermal controls on trace-element partitioning between coexisting garnet and biotite in metamorphic rocks from western Labrador: Canadian Mineralogist, v. 37, p. 443–468.

Yeo, G.M., and Delaney, G., 2007, The Wollaston Supergroup, stratigraphy and metallogeny of a Paleoproterozoic Wilson cycle in the Trans-Hudson Orogen, Saskatchewan: Geological Survey of Canada Bulletin 588, p. 89–117.